sedExnerFoam 2412: A 3D Exner-based sediment transport and morphodynamics model

Matthias Renaud[1,2], Cyrille Bonamy[1], Olivier Bertrand[3], and Julien Chauchat[4]

[1]Univ. Grenoble Alpes, CNRS, Grenoble INP, LEGI, 38000 Grenoble, France
[2]Chaire Oxalia – Fondation Grenoble INP, 46 Avenue Félix Viallet, 38000 Grenoble, France
[3]Artelia, 4 Rue Germaine Veyret-Verner, 38130 Échirolles, France
[4]Univ. Grenoble Alpes, INRAE, CNRS, Grenoble INP, IRD, IGE, 38000 Grenoble, France

Correspondence: Matthias Renaud (matthias.renaud@grenoble-univ-alpes.fr)

Abstract. Predicting the complex interplay between flow hydrodynamics, sediment transport and morphological evolution is a key challenge in hydraulic and coastal engineering. This paper presents an open-source numerical model for sediment transport and morphological evolution called *sedExnerFoam*. Implemented in the C++ multi-physics simulation toolkit *OpenFOAM*, the model combines high resolution hydrodynamics with a transport equation for suspended sediment concentration, as well as a morphological evolution module based on the Exner equation. The sediment bed is one of the computational domain's boundaries, and its geometry varies over time. In turn, the evolution of the bed position affects the hydrodynamics through mesh deformation. Following a thorough description of the model, a series of benchmark tests are presented to evaluate its performance and demonstrate its capabilities. These benchmarks consist of a set of simplified simulations designed to validate each model component independently. These include a turbulent suspension case in an equilibrium channel, a case in which the flow transitions from a rigid starved bed to an erodible bed, becoming progressively laden with suspended sediments, and an idealized dune migration scenario that is decoupled from flow hydrodynamics. Finally, two deposition tests validate the model's mass conservation capability and highlight the avalanche mechanism that prevents excessive bed slope steepness. After the model has been validated, an application to the migration of a single dune under the influence of a steady flow is presented. Incorporating spatial bedload flux saturation has been shown to be essential for achieving stable simulations and quantitative comparisons with experimental data in this application. The work presented in this manuscript represents a significant initial step in the development of a fully operational open-source model. Nevertheless, many improvements are still required before the model can be used in real applications, and some of these developments are listed in the 'Perspectives' section to guide future work.

1 Introduction

The transport of sediments and morphodynamics that is, the evolution of the sedimentary bed, is a complex physical problem involving many processes related to fluid mechanics, through the action of water on sedimentary particles, and solid mechanics when avalanches occur due to gravity. A coupling instability mechanism between fluid flow and bed evolution can also lead to the formation of bedforms, typically ripples or dunes (Kennedy, 1963; Charru et al., 2013). These bedforms alter the bed

roughness and create a feedback loop on the fluid flow, which can result in a significant increase in flood risk in rivers or estuaries (van der Sande et al., 2025; Hu et al., 2024). Therefore, morphodynamics models are essential tools for hydraulic engineers working on coastal, river, and estuarine systems, as they can be used to analyse erosion phenomena and assess the impact of human constructions, such as bridges, dams and renewable marine energy production systems (e.g. wind and tidal turbines).

The twentieth century saw the development of analytical models (Hjelmfelt and Lenau, 1970) and one-dimensional (1D) numerical models (Cunge et al., 1980; Goutal and Maurel, 2002) for the study of hydraulic and morphodynamic phenomena. In the 1980s and 1990s, two-dimensional (2D), depth-integrated and quasi-tridimensional numerical models emerged, primarily in the fluvial domain (Hervouet, 1999). Since the early 2000s, several three-dimensional (3D) models have been developed, including for coastal areas. Some are open-source, such as *openTELEMAC* (Benoit et al., 2002), *ROMS/CROCO* (Warner et al., 2008; Marchesiello et al., 2015) and *DELFT3D* (Lesser et al., 2004), while others are proprietary, such as *MIKE* (Warren and Bach, 1992). Most of these models are adapted to flows on 'large spatial and temporal scales', and are often based on the use of sigma coordinates in the vertical direction. This does not allow for the integration of obstacles such as bridge piers or wind turbine masts (Hervouet, 2007; Lesser et al., 2004). Another important approximation made in these models lies in the parametrization of the boundary layer: the first mesh point at the bottom is located in the logarithmic layer. Therefore these models are not particularly suitable for simulating interactions between morphodynamics and fluid flow around structures laid on the bottom, or for simulating processes such as scouring or bed instability, including the formation of ripples and dunes.

A new generation of 3D models based on emergent computational fluid dynamics (CFD) (Liu and García, 2008; Jacobsen, 2011; Baykal et al., 2015), allows for a finer resolution of flow and turbulence, particularly in the boundary layer and in the wake zones around structures. These models are based on the Arbitrary Lagrangian Eulerian (ALE) approach to handle the evolution of the bed boundary and the deformation of the associated volume mesh. To our knowledge, there is no open-source model of this type. While other approaches are possible, such as the immersed boundary method (IBM) (Song et al., 2022) or multiphase approaches (Chauchat et al., 2017; Nagel et al., 2020; Gilletta et al., 2024), these are too computationally expensive for engineering applications. The ALE method therefore seems to be the best compromise. As part of a collaboration between the University of Grenoble Alpes (CNRS, Grenoble INP and INRAE) and the engineering company ARTELIA Group, an open-source model is being developed within the C++ library *OpenFOAM®* (v2412) (Jasak et al., 2007). This model, named *sedExnerFoam*, is an ALE-based numerical model developed to support hydraulic engineering applications and in particular, to provide a relevant tool for studying scour around hydraulic structures. However, the model's scope extends to other applications, such as studying the formation and migration of bedforms in channels, assessing sediment deposition and erosion patterns in rivers, and analyzing sediment accumulation in reservoirs.

Scour is a specific sediment transport problem that requires fine local resolution in order to accurately capture the flow features around the obstacle (Song et al., 2022). To address this, the model relies on a CFD approach to solve the hydrodynamics and the excess of shear stress exerted on the sediment bed. This enables the study of various problems that cannot be simulated with depth integrated models or models that rely on boundary layer parametrization. For instance, the migration of steep bedforms with flow separation occurring at their lee side due to the adverse pressure gradient (van der Sande et al., 2025) (see

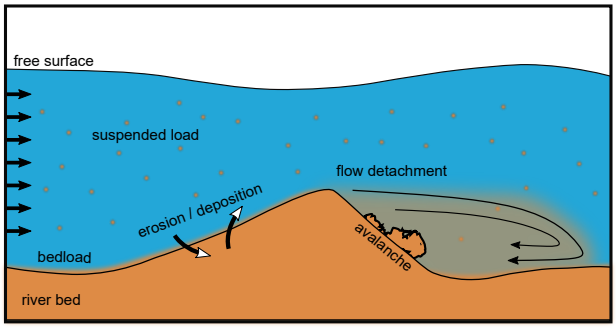

Figure 1. Schematic representation of the flow above a river bed and the main sediment transport processes involved.

Figure 1), or scour around a bridge pile and the horseshoe vortex which is the driving mechanism causing erosion upstream of the pile (Chiew and Melville, 1987; Roulund et al., 2005), or jet driven scour downstream of a sluice gate (Chatterjee et al., 1994; Martino et al., 2019).

After presenting the mathematical formulation of *sedExnerFoam* in Section 2 and the modeling approaches for hydrodynamics, turbulence, and sediment transport closures, several key numerical aspects are discussed in Section 3, with particular emphasis on the treatment of the Exner equation. This is followed, in Section 4, by the model validation against a series of academic benchmarks consisting of simple test cases designed to isolate individual components of the model and validate them separately against analytical solutions or experimental data. The validation suite includes simulations of idealized dune migration, sediment suspension under steady flow conditions, both in and out of equilibrium, and two sediment deposition scenarios. Finally, in Section 5, the model's capabilities are demonstrated through the simulation of an isolated dune migrating over a rigid bed under steady flow conditions. The numerical results reproduce a stationary migration regime, characterized by the dune moving at a constant velocity while maintaining its shape throughout the migration process. The conclusion provides a summary of the present work and discusses the current limitations of the model and possible future improvements.

2 Mathematical description

Sediment transport can be separated into two distinct modes: suspended load and bedload transport. Empirical formulas are used to estimate erosion and deposition fluxes between the riverbed and the water column, as well as the amount of sediment entrained in the bedload layer. This section provides a comprehensive overview of the model's components, beginning with hydrodynamics, turbulence modeling, and the transport of suspended sediment. It then introduces the Exner equation, which governs the evolution of the bed morphology. The various closure relations used to estimate the threshold of motion and bedload flux are described, together with the avalanche model and the treatment of bedload flux saturation. Finally, the coupling between the suspended load and the sediment bed is detailed through an erosion–deposition formulation based on the classical reference concentration.

2.1 Hydrodynamics

The fluid motion is governed by the incompressible, filtered Navier–Stokes equations:

$$\frac{\partial \boldsymbol{u}}{\partial t} + \nabla.(\boldsymbol{u} \otimes \boldsymbol{u}) = -\frac{1}{\rho_f}\nabla p + \boldsymbol{g} + \nabla.(2\nu \boldsymbol{S} + \boldsymbol{\tau_f}), \qquad \nabla.\boldsymbol{u} = 0, \tag{1}$$

where the operator $\otimes$ is the dyadic product, $\boldsymbol{u}$ the fluid velocity, p the fluid pressure, $\boldsymbol{g}$ the gravitational acceleration, ρ_f the fluid density, ν the fluid kinematic viscosity and $\boldsymbol{S} = \frac{1}{2}[\nabla \boldsymbol{u} + (\nabla \boldsymbol{u})^T]$ is the strain rate tensor. $\boldsymbol{\tau_f}$ is a tensor which definition depends on the type of filter used. It can either be the opposite of the specific Reynolds stress tensor to run Reynolds Averaged Simulations (RAS), a subgrid scale stress tensor when performing Large Eddies Simulations (LES) or the null tensor in case of laminar simulations or Direct Numerical Simulations (DNS). The model makes use of the vast panel of possibilities offered by *OpenFOAM* and let the user choose freely the kind of filtering to be applied to equation 1. In this work however, the numerical simulations presented are either laminar cases (no filtering of the Navier-Stokes equations) or unsteady RAS simulations.

At this stage of model development, no feedback of the suspended load on the hydrodynamics is considered, an assumption appropriate for dilute suspensions where density effects and particle drag are negligible.

2.2 Turbulence modeling

As stated previously, in the case of RAS filtering, the tensor $\boldsymbol{\tau_f}$ in equation 1 is equal to the opposite of the specific Reynolds stress tensor $\boldsymbol{\tau_f} = -\langle \boldsymbol{u'} \otimes \boldsymbol{u'} \rangle$, with $\langle\ \rangle$ the Reynolds operator and $\boldsymbol{u'}$ the fluctuating velocity field. A total of 6 additional unknowns (the velocity fluctuation correlations) are introduced in the system of equations by the use of the Reynolds stress tensor. The system as such is undetermined and the classical Boussinesq assumption is used as a closure. It expresses the Reynolds stress tensor as a function of the eddy viscosity ν_t and $k = \frac{1}{2}\langle \boldsymbol{u'}.\boldsymbol{u'} \rangle$, the turbulent kinetic energy (TKE):

$$\boldsymbol{\tau_f} = 2\nu_t \boldsymbol{S} - \frac{2}{3} k \boldsymbol{I_3}, \tag{2}$$

where $\boldsymbol{I_3}$ is the identity matrix. Then, a turbulence model is used to compute ν_t. *OpenFOAM* offers multiple turbulence models to users, many of which are two-equations based on k and either ϵ or ω, the rate of dissipation of TKE and the specific rate of dissipation of TKE respectively. A transport equation is then solved for each variable.

Of the various turbulence models available for the RAS approach in *OpenFOAM* ($k-\epsilon$, $k-\omega$, $RNG\,k-\epsilon$ ...), only the well-known $k-\omega$ Shear Stress Transport (SST) model is used in this work. The choice of this model was motivated by its capability to simulate both free shear flows and boundary layers, as well as its accuracy in capturing flow separation caused by adverse pressure gradients. It was first introduced by Menter (1994) and was initially derived for aerodynamics study. The $k-\omega$ SST consists of a combination of two other classical turbulence models, the $k-\epsilon$ (Launder and Spalding, 1983) and the $k-\omega$ (Wilcox et al., 1998) models. The aim is to take the best out of those two models. Indeed, the $k-\epsilon$ model is known to perform well for free shear flows but exhibits poor accuracy in the presence of adverse pressure gradients, rendering it unsuitable for flows involving boundary layer separation. Conversely, the $k-\omega$ model is better suited for capturing flows

with adverse pressure gradients and boundary layers, but it is less efficient than the $k-\epsilon$ for simulating free shear flows in regions outside the range of influence of the solid boundaries (e.g. rigid walls, sediment bed). The $k-\omega$ SST model transitions between the two models using blending functions that take the distance to the nearest wall as input. In the version implemented in *OpenFOAM*, the eddy viscosity ν_t is expressed as follows:

$$\nu_t = a_1 \frac{k}{\max(a_1\omega, b_1 F_{23} \|\boldsymbol{S}\|)}\,, \tag{3}$$

where $F_{23} = F_2 F_3$ is the product of two blending functions (F_2 and F_3) and $\|\boldsymbol{S}\| = \sqrt{2\boldsymbol{S} : \boldsymbol{S}}$ is a scalar measure of the strain rate tensor, with : the double inner product defined as $\boldsymbol{S} : \boldsymbol{S} = tr(\boldsymbol{S}\boldsymbol{S}^T)$, where tr is the trace operator. The temporal evolutions of k and ω are described by two transport equations:

$$\frac{\partial k}{\partial t} + \boldsymbol{u}.\nabla k = \tilde{P} - \beta_* k\omega + \nabla.((\nu + \alpha_k \nu_t)\nabla k)\,, \tag{4}$$

$$\frac{\partial \omega}{\partial t} + \boldsymbol{u}.\nabla \omega = \frac{\gamma}{\nu_t} P - \beta\omega^2 + \nabla((\nu + \alpha_\omega \nu_t)\nabla\omega) + 2(1-F_1)\alpha_{\omega 2}\frac{1}{\omega}\nabla k.\nabla\omega \tag{5}$$

where F_1 is another blending function. The production term P is defined as $P = \nu_t \nabla \boldsymbol{u} : [\nabla \boldsymbol{u} + (\nabla \boldsymbol{u})^T]$. In the equation for k (Eq. 4), a limiter is applied on the production rate:

$$\tilde{P} = \min\left(P, c_1 \beta_* k\omega\right)\,. \tag{6}$$

The different blending functions and constants of the model are detailed in Appendix A.

2.3 Suspended sediment transport

In *sedExnerFoam*, the suspended load is described by the suspended sediment volume fraction $c_s = V_s/(V_s+V_f)$ where V_s and V_f stand for the volume of sediment and the volume of fluid, respectively. The evolution of c_s in space and time is governed by an advection-diffusion equation:

$$\frac{\partial c_s}{\partial t} + \nabla.[(\boldsymbol{u} + \boldsymbol{w_s})c_s] = \nabla.(\epsilon_s \nabla c_s)\,, \tag{7}$$

where $\boldsymbol{w_s}$ is the sediment settling velocity and ϵ_s is the turbulent diffusivity for the suspended sediments. It is expressed as the ratio of the turbulent eddy viscosity and the Schmidt number σ_c as $\epsilon_s = \nu_t/\sigma_c$. The possibility to use an additional diffusivity ϵ_w in near bed areas is discussed in Section 2.4.3. The suspended sediments concentration is supposed to behave has a passive scalar being transported with the flow and settling due to the effect of gravity. The settling velocity is computed as follows:

$$\boldsymbol{w_s} = w_s^0 F_h(c_s)\,\boldsymbol{e_g}\,, \tag{8}$$

where w_s^0 is the terminal sediment settling velocity of a single particle in a quiescent fluid, $\boldsymbol{e_g} = \boldsymbol{g}/|\boldsymbol{g}|$ is a unit vector oriented with gravity, and F_h is an hindrance function that takes values between 0 and 1 and is a decreasing function of c_s. It represents

keyword	formula (for C_D or w_s^0)	references
	terminal fall models	
Stokes	$w_s^0 = \frac{1}{18\nu}(s-1)gd^2$	Stokes (1901)
Fredsoe	$C_D = 1.4 + \frac{36\nu}{w_s^0 d}$	Fredsoe and Deigaard (1992)
Soulsby	$w_s^0 = \frac{\nu}{d}\sqrt{10.36^2 + 1.049D_*^3}$	Soulsby and Whitehouse (1997)
Rubey	$w_s^0 = \left(\sqrt{2/3 + 36D_*^{-3}} - \sqrt{36D_*^{-3}}\right)\sqrt{(s-1)gd}$	Rubey (1933)
fixedValue	value given by user	
	hindrance models	
Zaki	$F_h(c_s) = (1-c_s)^n$	Richardson and Zaki (1954)
ZakiModified	$F_h(c_s) = (1-c_s)^{n-1}(1-c_s/c_s^{\max})^{c_s^{\max}}$	Camenen (2008)
fixedValue	value given by user	

Table 1. Different available options in *sedExnerFoam* to compute the terminal falling velocity w_s^0 and hindrance functions F_h. Models are selected in the file *suspensionProperties* using the entries *fallModel* and *hindranceModel*.

the effect of particles hindering each other as they fall leading to a drop of their settling velocity when c_s increases (Richardson and Zaki, 1954). The different models available to compute the terminal falling velocity w_s^0 and the hindrance function F_h are summarized in Table 1. The terminal settling velocity can be determined either directly from the fluid and sediment properties or implicitly through the drag coefficient C_D. Two of the available methods for estimating w_s^0 employ formulations based on the dimensionless diameter D_* (van Rijn, 1984) defined as follows:

$$D_* = d\left(\frac{(s-1)g}{\nu^2}\right)^{1/3}, \tag{9}$$

where $s = \rho_s/\rho_f$ is the density ratio, and ρ_s and ρ_f are the density of the sediment and the fluid respectively. The relationship between particle diameter and terminal settling velocity, as determined by the available closures, is shown in Figure 2.

The values adopted for the Schmidt σ_c number have remained a topic of debate to this day, with no consensus yet reached. van Rijn (1984) proposed a formula to estimate σ_c from the sediment settling velocity and the friction velocity u_*:

$$\sigma_c = \frac{1}{1 + 2\left(\frac{w_s}{u_*}\right)^2}, \quad \text{for} \quad 0.1 < \frac{w_s}{u_*} < 1\,. \tag{10}$$

This yields a Schmidt number smaller than one which corresponds to suspended sediment being dispersed more effectively than momentum is mixed by turbulence. This can be explained by the fact that turbulent diffusion is not the only mechanism

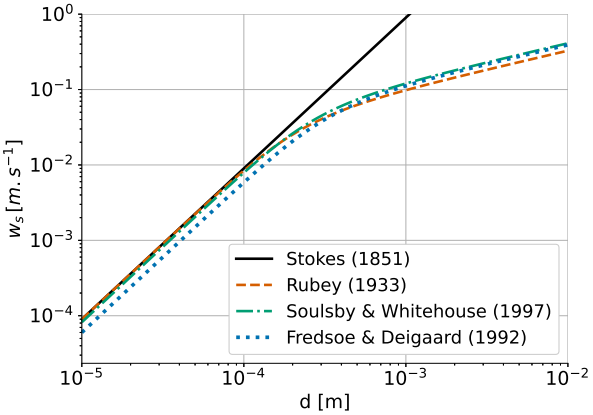

Figure 2. Different formulas to compute the terminal settling velocity of a sand particle ($\rho_s \approx 2650\,\mathrm{kg.m^{-3}}$) in water as a function of the grain size.

responsible for sediment dispersion, additional processes such as particle collisions, particle inertia, and lift forces can also enhance sediment diffusivity. Because these mechanisms are not accounted for in this classical approach, the Schmidt number is generally treated as a tuning parameter. In this model, the Schmidt number is treated as constant and defined by the user, with the preceding equation (Eq. 10) serving as a useful guideline for choosing its value.

The final key aspect of this approach is how to enforce the bed boundary condition, that is the exchange of mass between the sediment bed and the suspended load. This topic is covered in the Section (2.4.3) relative to erosion and deposition rates.

2.4 Bedload and Morphodynamics

Sediment transport modeling seeks to quantify how bedforms and channel morphology evolve under fluid flow. The section begins with the Exner equation description, which links bed elevation changes to sediment-flux divergence, followed by the motion threshold and bedload transport formulations that describe the onset and rate of particle motion. Slope-driven avalanching and bedload saturation further constrain near-bed dynamics, while erosion and deposition terms associated with suspended load exchange complete the framework for capturing morphodynamic evolution.

2.4.1 Exner equation

The morphological evolution of a granular bed in a wide range of sediment transport problems is modeled by the so-called Exner equation, which was first proposed by Exner (1920). In their article, Paola and Voller (2005) mention that Felix Exner initially suggested that the bed elevation was evolving proportionally with the divergence of the mean flow velocity but made clear that the mean flow acted as a proxy for the sediment flux. This led to the standard formulation, which is written as follows:

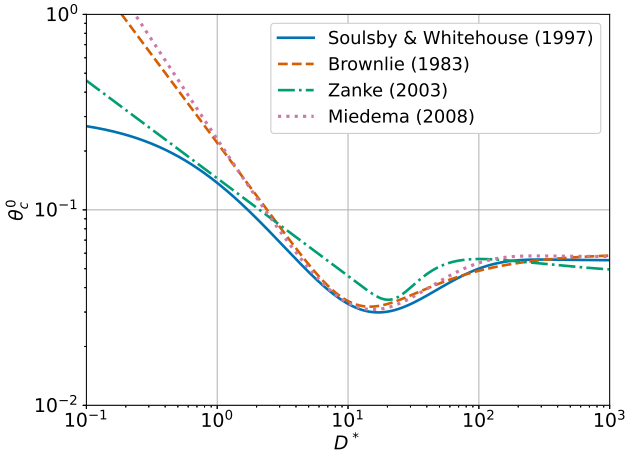

Figure 3. Critical Shields number as a function of the dimensionless sediment diameter D_*.

$$(1-\lambda_s)\frac{\partial z_b}{\partial t} + \nabla_H . \boldsymbol{q_b} = D - E\,, \tag{11}$$

where z_b is the bed elevation, λ_s is the porosity of the granular material which is linked to the maximum possible sediment volume fraction $c_s^{\max} = 1 - \lambda_s$. The bedload flux $\boldsymbol{q_b}$ is the specific flux of sediment transported along the bed per unit width. It is computed from the bed shear stress using an empirical formula. The formulas available to the user are all summarized in Table 2 and discussed in the next section. D and E are respectively the deposition and erosion rates, they are the terms through which sediment is exchanged between the bed and the water column. The Exner equation is a 2D equation and is thus solved after applying a 2D plane projection on all variables. The operator ∇_H stands for the divergence operator on this projected plane.

2.4.2 Bedload modeling

In the 1930's, Shields made measurements of the motion threshold already highlighted by Du Boys in 1879 (Hager, 2005). The particles start to move when the Shields number $\theta = \frac{|\boldsymbol{\tau_b}|}{(\rho_s - \rho_f) g d}$ exceeds a critical value θ_c, where $\boldsymbol{\tau_b}$ is the shear stress exerted by the flow on the bed. In his work, Albert Shields showed that the critical Shields number is Reynolds dependent leading to the development of various empirical formulas trying to estimate θ_c. Different formulations based on the dimensionless sediment particle diameter D_* (Eq. 9) have also been proposed in the literature such as in the work of Brownlie (1983) and Soulsby and Whitehouse (1997). The various formulas available in the model are summarized in Table 2 and represented in Figure 3. The user can choose between one of those models or manually set a value for θ_c.

Accurately measuring the threshold of motion is challenging, primarily because no universal definition exists. Different criteria, such as initial grain displacement, sustained motion, or measurable transport, lead to different threshold values. Furthermore, corrections need to be applied to the value of θ_c to account for bed slope effect. In the following, the base critical

keyword	formula	references
	critical Shields number	
Brownlie	$\theta_c^0 = \frac{0.22}{D_*^{0.9}} + 0.06\,10^{-7.7 D_*^{-0.9}}$	Brownlie (1983)
Miedema	$\theta_c^0 = \frac{0.2285}{D_*^{1.02}} + 0.0575(1 - e^{-0.0225 D_*})$	Miedema (2008)
Soulsby	$\theta_c^0 = \frac{0.3}{1+1.2 D_*} + 0.055\,(1 - e^{-0.02 D_*})$	Soulsby and Whitehouse (1997)
Zanke	$\theta_c^0 = \frac{0.145}{D_*^{0.5}} + 0.04510^{-1100 D_*^{-2.25}}$	Zanke (2003)
	bedload transport formulas	
Camenen	$\phi_b = 12\,\theta^{1.5} e^{-4.5\theta_c/\theta}$	Camenen and Larson (2005)
MeyerPeter	$\phi_b = 8\,\varpi(\theta - \theta_c)^{3/2}$	Meyer-Peter and Müller (1948)
Nielsen	$\phi_b = 12\,\theta^{1/2}\varpi(\theta - \theta_c)$	Nielsen (1992)
vanRijn	$\phi_b = 0.053 \frac{\varpi(\theta/\theta_c - 1)^{2.1}}{D_*^{0.3}}$	Van Rijn (1984)
custom	$\phi_b = \eta_b \theta^a \varpi(\theta - \theta_c)^b$	

Table 2. Available formulas to compute the critical Shields number from the fluid and sediments physical properties and formulas to compute the dimensionless bedload flux, also called Einstein number, from the Shields number. Those formulas are selected in the file *bedloadProperties* using the entries *criticalShieldsModel* and *bedloadModel*.

Shields number, which is the critical Shields number on a flat bed, is noted θ_c^0. The critical Shields number after slope correction is denoted by θ_c. Following Fredsoe and Deigaard (1992), a correction to account for the local bed slope is applied to the critical Shields number:

$$\frac{\theta_c}{\theta_c^0} = \cos(\beta_s)\sqrt{1 - \frac{\sin^2(\alpha_s)\tan^2(\beta_s)}{\mu_s^2}} - \frac{\cos(\alpha_s)\sin(\beta_s)}{\mu_s}\,, \tag{12}$$

where β_s is the angle of the bed slope and α_s the angle between the steepest slope direction and the direction of the shear. The coefficient of static friction μ_s is linked to the angle of repose of the granular material β_r through $\tan(\beta_r) = \mu_s$.

Various studies have focused on trying to find relationships between the Shields number and the dimensionless bedload flux $\phi_b = |\boldsymbol{q_b}|/\sqrt{(s-1)gd^3}$ (Einstein, 1942; Meyer-Peter and Müller, 1948; Van Rijn, 1984), leading to the development of numerous empirical relations. Many classical formulas (Meyer-Peter and Müller, 1948; Nielsen, 1992; Ribberink, 1998) are of the form:

$$\phi_b \propto \theta^a\,\varpi(\theta - \theta_c)^b\,, \tag{13}$$

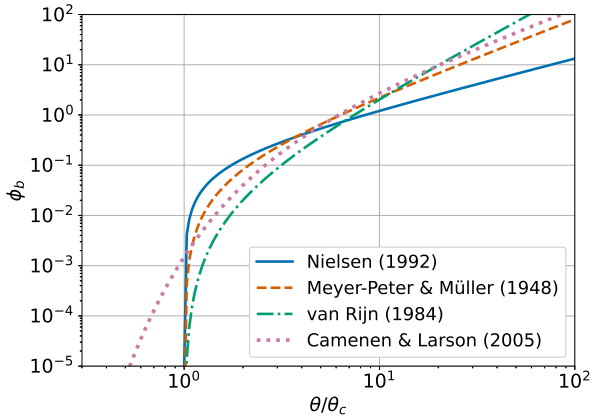

Figure 4. The dimensionless bedload flux as a function of the relative Shields number θ/θ_c from the empirical formulas detailled in Table 2.

with a and b, two real positive coefficients and ϖ the threshold function so that $\varpi(\theta-\theta_c)=\theta-\theta_c$ if $\theta>\theta_c$ and 0 else. In this work, the bedload flux $\boldsymbol{q_b}$ is aligned with the bed shear stress. The formulas available for the user to compute the bedload are summarized in Table 2 and represented in Figure 4. The user also has the possibility to define a custom bedload formula by manually setting the prefactor and the coefficients a and b in equation 13.

In addition to transport driven by bed shear stress, sediment can also be mobilized through local avalanche processes when the bed slope exceeds the angle of repose of the granular material. If not taken into account, unrealistic slopes could appear in the numerical solution or even shock situations which could trigger numerical instabilities in the model. Marieu et al. (2008) proposed a model based on an iterative procedure to redistribute the excess of sediment locally until the bed slope does not exceeds the granular material angle of repose. Such a procedure has been successfully tested in other works (Zhou, 2017). In *sedExnerFoam* however, the avalanche is modeled with an additional bedload term $\boldsymbol{q_{av}}$ inspired from Duran Vinent et al. (2019):

$$|q_{av}| = q_{av}^0 \frac{\varpi[\tanh(\tan(\beta_s)) - \tanh(\tan(\beta_r))]}{1-\tanh(\tan(\beta_r))}\,, \tag{14}$$

with β_s and β_r, the angle of the slope and the repose angle of the granular material, respectively. q_{av}^0 is a positive constant which can be set by the user. It corresponds to the maximum possible additional bedload flux due to the avalanche. This avalanche flux is oriented toward the steepest slope direction. One benefit of this formulation is that it enables slopes to exceed the angle of repose in the event of competition between bedload flux due to bed shear stress and that due to gravitational acceleration.

One last aspect which is often neglected when modeling sediment transport in water but is widely used in aeolian transport is the saturation of the bedload flux. From Charru (2006) and Charru et al. (2013) the saturation can be expressed in a coordinates system aligned with the shear stress as:

$$T_{sat}\frac{\partial q_b}{\partial t} + L_{sat}\frac{\partial q_b}{\partial x} = q_{sat} - q_b\,, \tag{15}$$

where $\boldsymbol{q_{sat}}$ is the saturated flux, T_{sat} the saturation time, L_{sat} the saturation length and x is the coordinate in the direction of the shear stress. When taking the saturation into account, the saturated flux $\boldsymbol{q_{sat}}$ is computed from the bed shear stress using one of the available formula presented in Table 2 and the bedload flux $\boldsymbol{q_b}$ is the solution of equation 15. Similar to the Exner equation, the saturation equation is solved on a horizontal plane after projection. A clear limitation is that this formulation is 1D, limiting its application to cases limited to one horizontal direction. To the authors' knowledge, no multidimensional extension of this equation has yet been reported in the literature.

2.4.3 Erosion and deposition rates

As mentioned earlier, the modeling of erosion and deposition fluxes represents one of the main challenges in classical sediment transport models. Many sediment transport experiments in straight flumes have been conducted to study the relation between the flow and the rate at which particles are eroded from the bed to the water column. In his work, van Rijn (1984) studied the case of sediment transport in a straight channel under equilibrium condition and proposed an empirical formula to compute a reference concentration c_b^* at a certain reference distance from the bed, the so-called reference level δz_b^*:

$$c_b^* = 0.015 \frac{d}{\delta z_b^*} \frac{(\theta/\theta_c - 1)^{3/2}}{(D_*)^{0.3}}. \tag{16}$$

The reference concentration corresponds to the concentration observed at a distance δz_b^* from the bed under equilibrium condition.

This development has been adopted in many sediment transport models, which assume equilibrium at the reference level to define the boundary condition $c_s(\delta z_b^*) = c_b^*$. However, this boundary condition is not suitable for cases in which the assumption of local equilibrium at the reference level does not hold. It was adapted by Celik and Rodi (1988) to accommodate non-equilibrium conditions. The erosion rate is written $E = w_s c_b^*$ and the deposition rate $D = w_s c_b$, with c_b a sediment concentration value computed from the values in the neighboring cells which is detailed later on. The erosion rate is assumed equal to its equilibrium value, while deposition depends only on the concentration in the first cells above the bed. If $c_b > c_b^*$, then suspended sediment get deposited on the bed and when $c_b < c_b^*$, sediment get eroded from the bed and suspended in the water column. The equilibrium occurs when $c_b = c_b^*$.

One difficulty lies in prescribing the reference concentration at the reference level, which is located at some distance above the bed boundary. Large scale sediment transport models avoid this difficulty by not meshing the region located in between the sediment bed and the reference level. The downfall of this method being that the flow near the bed is not solved and need to be modeled, typically leading to a bad hydrodynamics in highly non uniform flow regions such as near obstacles. In order to maintain a good hydrodynamics resolution, Jacobsen (2011) developed a model relying on a different mesh for the hydrodynamics and for the suspended load. The bottom boundary of the mesh for the suspended load was located at the reference level whereas the mesh for the hydrodynamics presented cells in between the sediment bed and the reference level. In *sedExnerFoam*, the choice to use a single mesh was made primarily for practical reasons, to simplify the operation of the model by avoiding the use of two different meshes and by allowing all boundary conditions to be applied directly at the bed interface.

As stated previously, the deposition and erosion fluxes are computed as suggested by Celik and Rodi (1988). The erosion E is computed at the reference level $\delta z_b^* = k_s$, the Nikuradse equivalent roughness height ($k_s = 2.5d$), using equation 16 and a limiter so that c_b^* is not exceeding a value $c_{b,max}^*$, typically equal to half the maximum possible sediment volume fraction. This limiter is needed to avoid c_b^* taking non physical values when the bed shear stress becomes important (see Eq. 16). In their work Amoudry et al. (2005) use a maximum possible reference concentration $c_{b,max}^* = 0.3$ which is close to the value of 0.32 suggested by Engelund and Fredsøe (1976). The computed reference concentration is then extrapolated at the height of the first cell center above the sediment bed boundary z_1, using the formula suggested by Fang and Rodi (2003):

$$c_{b1}^* = min\left(c_b^* e^{-\frac{w_{s1}}{\epsilon_{s1}}(z_1 - \delta z_b^*)}, c_{b,max}^*\right), \tag{17}$$

where c_{b1}^* is the reference concentration extrapolated at the height z_1. w_{s1} and ϵ_{s1} stand for the settling velocity and the sediment turbulent diffusivity values at the center of the first cell above the sediment bed located at a height z_1. The expression of c_{b1}^* is obtained by considering a local equilibrium in a small region above the bed and assuming ϵ_s and w_s to be uniform between the reference level δz_b^* and the center of the first cell above the bed. The deposition and erosion are then computed at the first cell center and not on the bed boundary, leading to $D = w_s c_1$. The total erosion/deposition rate is then estimated as:

$$D - E = w_{s1}(c_1 - c_{b1}^*)\,. \tag{18}$$

This flux is prescribed as a boundary condition for the suspended-load transport (Eq. 7). With this approach, the same computational mesh can be employed for both suspended-load and hydrodynamic calculations, allowing for fine resolution near the sediment bed. It should be noted that the various formulations for c_b^* found in the literature are empirical in nature and are derived primarily from measurements conducted in straight-channel flow experiments. Their applicability outside of such configurations, particularly in the vicinity of obstacles that disturb the flow, should therefore be treated with caution.

To address difficulties in suspending material from the bed to the water column under fine grid resolution and low roughness Reynolds number conditions $k_s^+ = \frac{k_s u_*}{\nu}$, an additional near-bed diffusivity for suspended sediments ϵ_w, was introduced in the model. In the smooth and intermediate roughness regimes, the eddy viscosity vanishes within a thin layer near the bed. When the mesh resolution is sufficiently fine such that the first cells lie within this layer, the eroded sediment tends to remain confined to these cells rather than being transported upward into the water column. To mitigate this issue, an additional artificial diffusivity is introduced in the near-bed region:

$$\frac{\epsilon_w}{\nu} = \frac{\epsilon_w^0}{2}\left(1 - \tanh\left(\xi_w \frac{z - k_s}{k_s}\right)\right). \tag{19}$$

It can be interpreted as the dispersion resulting from particle collisions, which is not accounted for in equation 7 but plays a role locally in the near-bed region, where the solid volume fraction can be significant. This term allows particles to reach an elevation above the viscous sublayer, where they can be entrained by turbulent eddies and transported upward into the water column. However, when the flow is hydraulically rough ($k_s^+ \geq 90$), turbulence penetrates down to the bed, and the use of ϵ_w is no longer necessary. The coefficients ϵ_w^0 and ξ_w are both set to 5 by default.

3 Numerical implementation

The numerical implementation of *sedExnerFoam* is based on the finite volume method (FVM) and developed within the *OpenFOAM*® (v2412) framework. The development originated from the existing solver *pimpleFoam*, which is designed for incompressible transient flow simulations and employs the PIMPLE algorithm for pressure-velocity coupling. This section outlines the key numerical features of the model, its operating sequence, and the numerical methods employed, with particular attention given to the treatment of the Exner equation. Finally, the case structure is presented, including all necessary files and the modeling options available to users.

3.1 Code implementation

The Navier-Stokes equations (Eq. 1) and the transport equation for suspended load (Eq. 7) are both solved using the finite volume method. The computational domain is discretised into a multitude of discrete polyhedral control volumes over which the partial differential equations are integrated. The Exner equation, however, is solved over a surface (the sediment bed) using the finite area method (FAM). FAM is an adaptation of the finite volume methods on a surface curved in the 3D space. It was initially developed by Tukovic and Jasak (2008) for the numerical study of the transport of a surfactant at the interface between two fluids and has since then been successfully applied to other problems such as dense-flow avalanches (Rauter and Kowalski, 2024). In the present model, the finite area mesh is coupled with the volumetric mesh patch representing the sediment bed, such that the finite area mesh coincides with the bed boundary of the finite volume mesh. This approach ensures seamless interaction between flow and sediment transport without the need for multiple meshes. The partial differential equations discretization with the finite area method was initially developed to take into account the curvature of the surface, however no curvature effect is taken into account for the bed morphology evolution. The Exner equation is solved on a projected plane normal to the gravity vector $\boldsymbol{g}$.

The sequence of operations performed during a time iteration and their sequence is represented in Figure 5. After solving the mesh deformation, the differential equations for the velocity field $\boldsymbol{u}$, the pressure p (Eq. 1) as well as transport equations for fields related to turbulence modeling (Eq. 4, 5) are first solved through the PIMPLE algorithm for transient solution which is detailed in Greenshields and Weller (2022). It consists in a mix of the SIMPLE (Semi-Implicit Method for Pressure-Linked Equations) from Patankar and Spalding (1983) and the PISO (Pressure Implicit with Splitting of Operators) from Issa (1986). An additional corrector loop called PIMPLE loop is added above the PISO loop. During each time step, the velocity flux through the mesh faces is updated at every PIMPLE loop iteration, preserving the simulation stability at higher Courant number ($C_o > 1$). The PISO algorithm behavior is restored by disabling the PIMPLE loop. Once the hydrodynamics has been solved, the shear stress exerted on the bed is computed as well as the associated bedload and erosion flux. The transport equation for suspended sediment transport is solved and the deposition flux is deduced from it. Lastly the bed boundary motion is computed by explicitly solving the Exner equation. At the beginning of the next time iteration, the mesh is updated to match the new bed position.

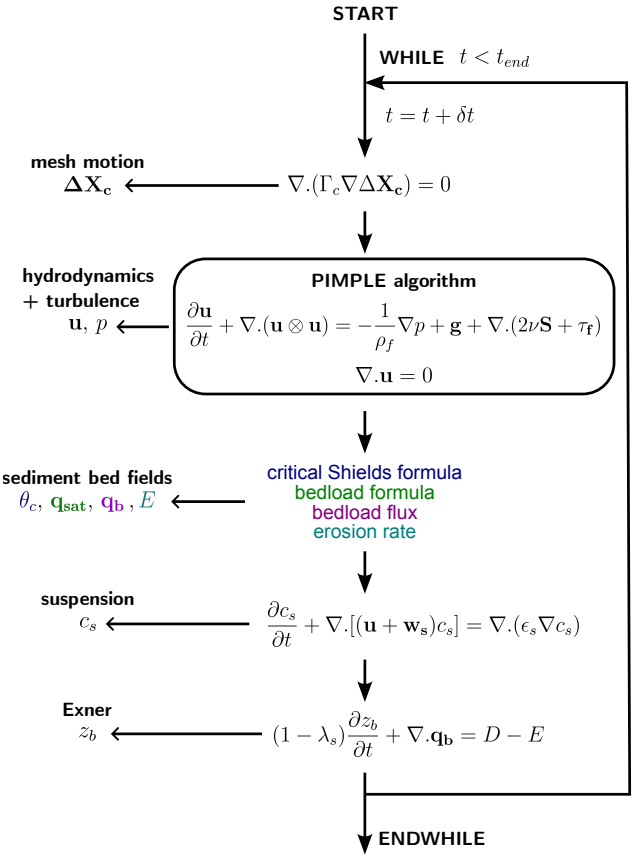

Figure 5. Flow chart of *sedExnerFoam*.

3.2 Exner equation resolution

Let us integrate the Exner equation (Eq. 11) over the projection of a face f:

$$\left.\frac{\partial z_b}{\partial t}\right|_f = -\frac{1}{S_{fp}} \sum_e (\boldsymbol{q_{b,ep}}.\boldsymbol{n_{ep}}) l_{ep} + (D - E)_f \,, \tag{20}$$

where $S_{fp} = S_f(\boldsymbol{n_f}.\boldsymbol{e_g})$ is the projected area of face f and S_f is face f area, $\boldsymbol{n_f}$ is the face normal unit vector oriented outward of the computational domain and $\boldsymbol{e_g}$ is a unit vector oriented along the gravity vector. l_{ep} is the length of the projected edge and $\boldsymbol{n_{ep}}$ the projected normal edge vector, oriented outward with respect to face f. The users have the choice to use either a explicit Euler scheme or a second order Adams-Bashforth scheme for temporal discretization.

From equation 20, at each time step, an increment of bed elevation δz_b is computed for each face centers. In *OpenFOAM*, the mesh geometry is defined by the vertices coordinates. Thus, to impose a mesh motion, the vertical displacements computed at face centers need to be interpolated on the vertices. Particular caution must be given to the interpolation scheme to ensure mass conservation. A straightforward approach would be to linearly interpolate z_b from face centers to vertices. Although

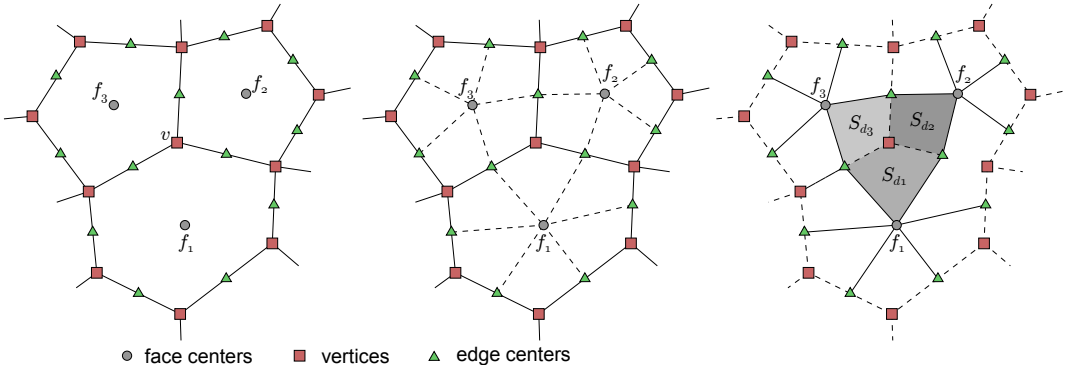

Figure 6. Decomposition of the horizontal projection of the finite area mesh into a dual mesh.

this method is mass-conservative for 1D cases on a structured mesh, it fails to preserve mass in the general 3D case with an unstructured mesh. Jacobsen (2015) provided a detailed review of the various methods available for solving the Exner equation and analyzed their respective advantages and limitations. He proposed a mass-conservative interpolation scheme, which is the one implemented in the present model.

A dual mesh is constructed as depicted in Figure 6. Each vertex v of the primary mesh serves as the center of a face in the dual mesh. The vertices defining this dual face consist of the neighboring primary faces f_i that share vertex v as well as the centers of the edges for which v is an endpoint. The mass increment of the sediments contained under a face f is $m_f = \rho_s S_{fp} \delta z_b|_f$, where $\delta z_b|_f$ is the face elevation increment. To ensure mass conservation during the interpolation process, the sum of the mass contained under every faces must be the same when computing this sum for the initial mesh and for the dual mesh. The vertical displacement of each vertex $\delta z_b|_v$ is then a linear combination of the displacements of the faces sharing this vertex. The weight associated with each face is proportional to the area of the quadrilateral defined by the face center, the vertex and the centers of the two edges belonging to the face and sharing the vertex (see Figure 6). Let us note the area of this quadrilateral S_{df}, the value of the elevation increment $\delta z_b|_v$ associated to a vertex v is computed:

$$\delta z_b|_v = \frac{1}{S_v} \sum_f S_{df} \delta z_b|_f \,, \tag{21}$$

where S_v is the area of the dual face whose center is the vertex v. It is equal to the sum of the area of each face associated quadrilateral: $S_v = \sum_f S_{df}$. Thus, the sum of the interpolation weights is equal to 1. This interpolation method is mass conservative and also serves as a filter. The final bed displacement at each face is computed in two steps: first, interpolation from faces to vertices, and then from vertices back to faces, with the face centers defined as the center of mass of the vertices composing each face. This filtering effect contributes to maintaining the numerical stability of the Exner equation solution.

3.3 Mesh motion

At each time step, solving the Exner equation gives a displacement for the bed boundary of the finite volume mesh. In order for the finite volume mesh to adapt to the bed boundary motion and to preserve the mesh quality throughout the simulation, a

mesh motion solver based on a laplacian equation for cell center displacements is used:

$$\nabla.(\Gamma_c \nabla \boldsymbol{\Delta X_c}) = 0\,, \tag{22}$$

where Γ_c is the mesh diffusivity and $\boldsymbol{\Delta X_c}$ is the displacement of the cell centers. Solving equation 22, new positions of the mesh cell centers are obtained. The mesh vertices new coordinates are then interpolated from $\boldsymbol{\Delta X_c}$. The motion solver is defined in the file *constant/dynamicMeshDict*, and this study utilizes the *displacementLaplacian* solver.

Using a spatially non-uniform mesh diffusivity (Γ_c) makes it possible to prioritize mesh quality and control cell sizes in specific regions. Areas with lower Γ_c are more prone to mesh distortion, whereas regions with higher values help prevent excessive cell shrinking or expansion, provided that bed movement remains moderate. Several approaches are available for prescribing Γ_c, giving the user flexibility in defining its spatial distribution. As a general guideline, it is recommended to assign a high mesh diffusivity near the sediment bed interface to preserve mesh quality in this critical region. The following options, which can be selected in the configuration file *constant/dynamicMeshDict*, ensure this behavior:

- inverseDistance: $\Gamma_c = 1/l_{sb}$
- quadratic inverseDistance: $\Gamma_c = 1/l_{sb}^2$
- exponential: $\Gamma_c = e^{-l_{sb}}$

where l_{sb} is the distance to the sediment bed boundary.

One drawback of using the finite-volume method to compute mesh motion is the need to interpolate vertex displacements from the cell centered displacements obtained from Eq. 22. This interpolation step can degrade mesh quality in regions where bed motion is highly non-uniform. In the worst-case scenario, severe distortion may cause some cells to collapse, ultimately leading to simulation failure. Among all the simulations conducted, one problematic case has been identified: the migration of a steep bedform. When the crest is sharp, the vertices located just above the crest, but not belonging to the bed boundary, may be displaced below the bed surface during the interpolation step. Reducing the aspect ratio of the near bed cells has proven to be an effective way to mitigate this issue.

In their work, Jasak and Tukovic (2006) examined in greater detail the issues that arise when mesh motion is computed using a finite-volume based approach. They proposed a vertex-based method that avoids cell-collapse problems during mesh deformation. To apply this method to meshes composed of arbitrary polyhedra, each polyhedron is decomposed into a set of tetrahedra. The drawback of this approach is that Eq. 22 must then be solved on a significantly refined tetrahedral mesh, which contains many more cells than the original. For instance, decomposing a hexahedral mesh increases the number of cells by a factor of six. For this reason, and because the classical finite-volume formulation has provided satisfactory results in practice, the vertex-based method is not currently implemented in *sedExnerFoam*. Nevertheless, it could be introduced in the future should the need arise for more demanding applications.

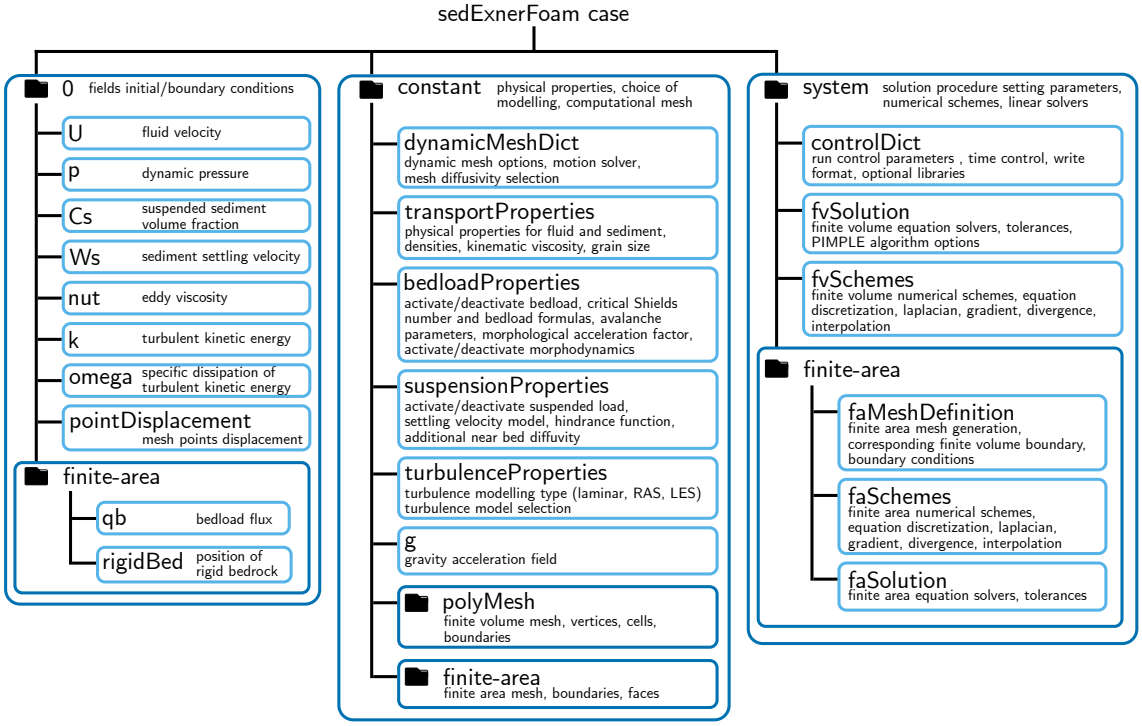

Figure 7. Case directory structure.

3.4 File structure of a case

The numerical setup is defined through a set of input files that specify the computational domain, physical parameters, boundary and initial conditions, and numerical options. Each file must be properly configured by the user before running the simulation. The following sections describe the purpose and required content of each file. The basic directory structure—i.e., all files required to run a *sedExnerFoam* simulation—is shown in Figure 7. It is organized into three main folders.

3.4.1 Initial and boundary conditions

The initial time directory, usually named 0 contains the initial conditions for all fields required by *sedExnerFoam*. Each field file defines both the initial field values and the boundary conditions applied to every patch of the mesh. The required fields include velocity (U), pressure (p), and, depending on the turbulence model employed, the relevant turbulent quantities. In Figure 7, the setup illustrates the use of the $k-\omega$ SST turbulence model and consequently, the additional turbulent fields required are ν_t (nut), k and ω (omega). The suspended sediment volume fraction (Cs) and settling velocity (Ws) must also be specified. The *finite-area* subdirectory contains the finite-area fields, including the bedload flux and, optionally, the position of a rigid bedrock. When a rigid bedrock is specified, the model restricts erosion to a predefined depth, ensuring that the non-erodible

layer remains unaffected. The initial time directory is read at the start of a simulation, providing the baseline from which the solution begins to evolve.

3.4.2 Constant directory

The *constant* directory contains the model configuration and physical properties, as well as the finite-volume and finite-area meshes stored in the *polyMesh* and *finite-area* subdirectories, respectively. The turbulence modeling approach (LES, RAS), and the specific model used, is defined in the *turbulenceProperties* file. Additionally, the *dynamicMeshDict* file is used to select the mesh-motion solver and the mesh-diffusivity method to be applied. The fluid and sediment properties, such as densities, grain size, and fluid kinematic viscosity, are specified by the user in the *transportProperties* file. Modeling options related to sediment transport are separated into two files, *suspensionProperties* and *bedloadProperties*, each corresponding to one mode of sediment transport.

In *suspensionProperties*, the user can enable or disable suspended load, select a settling-velocity and/or hindrance model (see Table 1), apply an additional wall diffusivity (see Eq. 19), and adjust the coefficients ϵ_w^0 and ξ_w, as well as the limiter on the reference concentration $c_{b,max}^*$ (see Eq. 17).

In *bedloadProperties*, the user can enable or disable bedload transport and morphological evolution, choose models for the critical Shields number and for the bedload formulation (see Table 2), activate the critical Shields number slope correction (Eq. 12), set the avalanche coefficient q_{av}^0, use a morphological acceleration factor, and specify whether a rigid, non-erodible bed exists beneath the sediment layer, which limits the maximum erosion depth.

3.4.3 Case run control

The system directory in *OpenFOAM* contains files that control how simulations are executed. Among them, the *controlDict* file specifies the simulation time controls, including start and end times, time-step settings, and also defines optional libraries and post-processing utilities to be executed during the simulation. The *fvSchemes* file, which specifies the numerical discretization schemes, and the *fvSolution* file, which sets the linear solvers and algorithmic controls. Depending on the case setup, additional configuration files may appear in this directory. The *finite-area* subdirectory contains all files related to the finite-area method, including its definition in *faMeshDefinition* and the numerical schemes and linear solvers in *faSchemes* and *faSolution*, respectively. Together, these files govern the computational parameters, numerical methods and overall runtime behavior of the simulation.

4 Model validation

A series of tests is presented both to illustrate the model behavior of *sedExnerFoam* and to validate it against either analytical solutions or experimental results. The tests are chosen to isolate one physical process at a time. They are organized as follows: two tests involving suspended load transport only are first presented (1D and 2D). Then the case of an idealized dune transport problem (1D) for which an analytical solution exists is investigated. At last, the conservation of mass is illustrated by means of

test	1565	1965	2565	1957
$d\,(\mathrm{mm})$	0.15	0.19	0.24	0.19
$w_s\,(\mathrm{cm.s^{-1}})$	1.6	2.3	3.1	2.3
$\overline{u}\,(\mathrm{m.s^{-1}})$	0.649	0.671	0.744	0.672
$H\,(\mathrm{cm})$	6.45	6.51	6.54	5.72
$u_*\,(\mathrm{cm.s^{-1}})$	3.58	3.75	4.25	3.95
R_o	1.09	1.24	1.38	1.17

Table 3. Parameters of four tests from Lyn (1988) experiment. Particles diameter d, settling velocity $\boldsymbol{w_s}$, mean water velocity $\overline{u}$, water depth, friction velocity u_* and Rouse number R_o.

two tests on suspended sediment deposition and avalanches (1D and 2D). Most of these tests are part of a continuous integration process available on the GitHub repository.

4.1 Suspension under equilibrium condition

A classical test is the suspension of sediment in a straight flume under equilibrium condition which has been extensively studied (van Rijn, 1984; Lyn, 1988; Muste et al., 2005). A fully developed flow in a channel is considered. The channel is supposed long enough so that the vertical profiles of velocity and turbulent eddy viscosity are stationary. Under equilibrium condition, the vertical profile of suspended sediment concentration is the results of a balance between the gravity which makes the particles to settle at a velocity $\boldsymbol{w_s}$ and the mixing induced by turbulence. The transport equation for the suspended load (Eq. 7) then reduces to:

$$\frac{d}{dz}\left(-w_s c_s + \epsilon_s \frac{dc_s}{dz}\right) = 0\,. \tag{23}$$

Depending on the shear stress exerted on the bed, granular material is eroded and suspended in the water column. Then, the turbulent diffusion uplifts the particles until an equilibrium is reached. Assuming a parabolic turbulent viscosity profile, $\nu_t(z) = u_*\kappa z(H-z)$, where $\kappa = 0.41$ is the von Kármán constant, the solution of equation 23 between the reference level δz_b^*, where the concentration is the reference concentration c_b^*, and the top of the water column H is the so-called Rouse profile:

$$c_s(z) = c_b^*\left(\frac{H-z}{z}\frac{\delta z_b^*}{H-\delta z_b^*}\right)^{R_o}, \tag{24}$$

where $R_o = \sigma_c w_s/\kappa u_*$ is the Rouse number.

To validate the model, numerical results are compared with experimental data from Lyn (1988). The experiment was conducted in a 13 meters long and 26.7 centimeters wide flume with a bottom covered by a layer of sand. Flow and suspended sediments concentration measurements were made approximately 9 meters downstream of the channel entrance. The experiment parameters are summarized in Table 3. For the four tests, measurements of the velocity field, the velocity correlation and the suspended sediment concentration profiles are available.

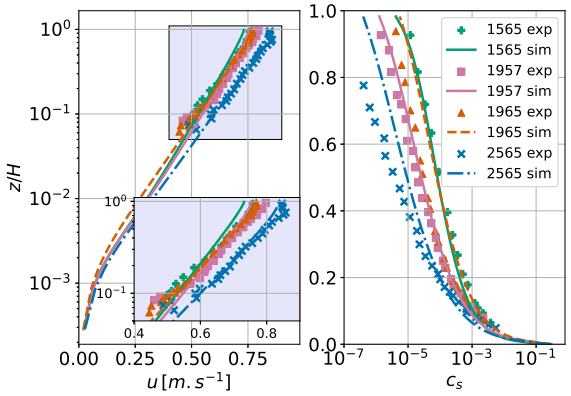

Figure 8. Velocity and suspended sediment concentration profiles from simulations and comparison with experimental data from Lyn (1988).

The four equilibrium bed experiments are reproduced numerically. A 1D mesh is employed, consisting of a column of 120 cells oriented along the vertical z-direction. Cyclic boundary conditions are applied in the stream wise x-direction, and the mesh is refined near the bed. Only the x-component $\boldsymbol{u}$ of the velocity field is non-zero. For all four simulations, the $k-\omega$ SST turbulence model is employed, and the mesh resolution near the bed is maintained at $z^+ \approx 1$ to ensure adequate resolution and an accurate estimation of the bed shear stress. Here, $z^+ = u_* z_1/\nu$ denotes the distance of the first cell center from the bed boundary in wall units, where z_1 is the distance to the sediment bed boundary.

The free surface is not considered, instead a rigid lid is applied at the top, with zero gradient condition for the turbulent kinetic energy k, a Dirichlet condition for ω and a slip boundary condition for the velocity $\boldsymbol{u}$. To take into account the bed roughness effect on the hydrodynamics, the boundary condition for ω proposed by Wilcox et al. (1998) is used:

$$\omega = \frac{u_*^2}{\nu} S_R \,, \tag{25}$$

where S_R is defined as a function of the roughness Reynolds number $k_s^+ = u_* k_s/\nu$ as follows:

$$S_R = \left(\frac{200}{k_s^+}\right)^2 \qquad \text{for } k_s^+ \leq 5 \,, \tag{26}$$

$$S_R = \frac{100}{k_s^+} + \left[\left(\frac{200}{k_s^+}\right) - \frac{100}{k_s^+}\right] e^{5-k_s^+} \qquad \text{for } k_s^+ > 5 \,. \tag{27}$$

The transient problem is solved and the simulations are run until a steady state has been reached. The numerical results are plotted alongside the experimental data from Lyn (1988) in Figure 8. Overall, the numerical results show good agreement with the experimental data. For the suspended sediment profiles, it is observed that in cases 2565 and 1957 the suspended sediment concentration is slightly overestimated, particularly in the upper part of the water column. To qualitatively assess the agreement between the numerical and experimental profiles, the symmetric mean absolute percentage error (SMAPE) of the logarithm of

the sediment volume fraction is computed as follows:

$$\text{SMAPE} = \frac{2}{N} \sum \frac{|\log_{10}(c_s^{\text{num}}) - \log_{10}(c_s^{\text{exp}})|}{|\log_{10}(c_s^{\text{num}})| + |\log_{10}(c_s^{\text{exp}})|}, \tag{28}$$

where N is the number of measurement available in the experimental test considered, c_s^{exp} is the experimental sediment volume fraction and c_s^{num} is the sediment volume fraction obtained from the numerical simulation and linearly interpolated to the elevations corresponding to the experimental data. The resulting errors are 4.34% for case 1565, 8.29% for case 1965, 6.64% for case 2565, and 2.46% for case 1957. These results were obtained without any calibration of the model coefficients, and an improved fit could likely be achieved by adjusting parameters such as the turbulent Schmidt number σ_c, the near-bed diffusivity coefficients ϵ_w^0 and ξ_w (Eq. 19), or the equivalent sand roughness height k_s.

These simulations complete in a few seconds on a single CPU core.

4.2 Suspension development

Another test for the suspended load is the development of suspension in a channel, when the flow encounters an abrupt transition from a non erodible bed to an erodible bed. Initially, the flow is clear, and it becomes loaded with sediments until an equilibrium is reached. For this problem, the results are compared with a pseudo-analytical solution derived by Hjelmfelt and Lenau (1970). In order to obtain this solution, some hypotheses are made.

1. The sediment is uniformly advected at the mean flow velocity $\overline{u}$.
2. The turbulent viscosity vertical profile is assumed parabolic, $\nu_t = \kappa u_* z(1 - z/H)$ for $z \in [\delta z_b^*, H]$ where δz_b^* is the reference level and H, the water depth.
3. The concentration at $z = \delta z_b^*$ is supposed to be constant along the flume and equal to c_b^*, the reference concentration.
4. The horizontal turbulent diffusion is neglected.

Based on those hypothesis, Hjelmfelt and Lenau (1970) simplified the transport equation for the suspended-load and derived an analytical solution. They performed a separation of variable and used the Sturm Liouville theory to obtain a solution which only depends on the Rouse number. A first numerical simulation is performed for which all assumptions apart from the fourth one are respected. A water depth of $H = 0.1\,\text{m}$ is considered, the mean velocity is $\overline{u} = 0.9\,\text{m.s}^{-1}$ and the Rouse number is equal to 0.5 which corresponds to a regime in which suspended load is the dominant sediment transport mode. The results are presented in Figure 9.

In this case, the numerical and pseudo-analytical solutions are almost identical suggesting that the stream-wise turbulent diffusivity (hypothesis 4) is indeed negligible. However, some of the hypothesis from Hjelmfelt and Lenau (1970) are normally not verified. The vertical velocity profile is not uniform, the concentration at the reference level may vary in space and reach an equilibrium after some distance from the inlet and last the turbulent eddy-viscosity profile is not exactly parabolic.

The particle diameter was set to $d = 0.12\,\text{mm}$, corresponding to a settling velocity of $w_s = 0.773\,\text{cm.s}^{-1}$ and a Rouse number of $R_o = 0.5$. Although tests were conducted with different Rouse numbers, only the case $R_o = 0.5$ is presented in this

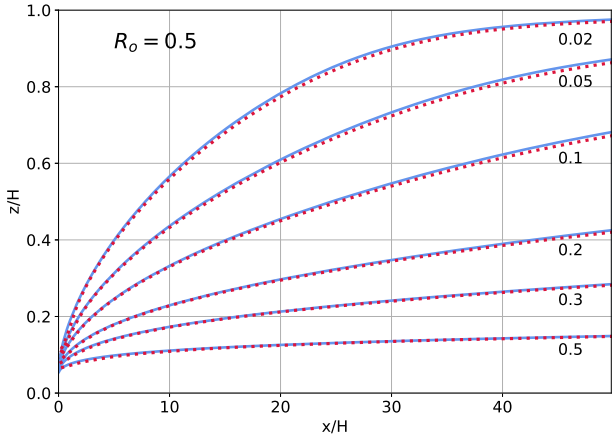

Figure 9. Isolines of c_s/c_b^* for a Rouse number of 0.5 with hypothesis from Hjelmfelt and Lenau (1970) enforced except the null horizontal turbulent diffusion. Solid blue curves represent the model results and the dotted red ones the pseudo analytical solution.

work. The same mean flow velocity $\overline{u} = 0.9\,\mathrm{m.s^{-1}}$ is taken and the resulting shear stress exerted on the bed corresponds to the bed friction velocity $u_* = 3.77\,\mathrm{cm.s^{-1}}$. The $k-\omega$ SST turbulence model and the rough wall boundary from Wilcox et al. (1998) (Eq. 25) condition is used for ω with a roughness height $k_s = 2.5\,d$.

A first 1D simulation is performed without sediment to obtain vertical profiles for $\boldsymbol{u}$, k and ω corresponding to a fully developed channel flow. The fields $\boldsymbol{u}$, k and ω are extracted from this first simulation and used as the inlet boundary condition for the second simulation for which suspension is activated. The flow entering the domain being already fully developed, only c_s varies with the x-position. The mesh consists in a 2D structured mesh more refined close to the bed to ensure the condition $z^+ \approx 1$ ($n_x = 2000$, $n_z = 100$). Isolines of c_s/c_b^* values from the model and the pseudo-analytical solution are presented in Figure 10. To compute the pseudo-analytical solution, the reference level was chosen equal to $\delta z_b^* = 0.05H$ as in the work of Hjelmfelt and Lenau (1970) and the reference concentration is taken equal to $c_b^* = 0.025$ and applied as a boundary condition at the elevation $z = \delta z_b^*$.

Compared with the situation where the hypothesis on the flow are enforced (see Figure 9), the model results do not match the pseudo analytical solution but the global behavior remains the same. Starting from no suspension, the suspended sediment quantity gradually increases with the distance to the inlet until reaching an equilibrium situation where the settling and the turbulent diffusion cancel each other out. Figure 11 shows the vertical suspended sediment volume fraction c_s profiles at different positions along the channel and shows the convergence toward an equilibrium solution close to a Rouse profile.

As stated previously, the discrepancies with the pseudo-analytical solution arise from the unrealistic assumptions made in its derivation. These include the assumption that suspended sediments are advected by the mean flow, the use of a parabolic eddy viscosity profile, and the assumption of local equilibrium at the reference level. A better agreement could yet be found, for instance by playing with the boundary conditions for ω at the top and bottom boundaries which would affect the shape of

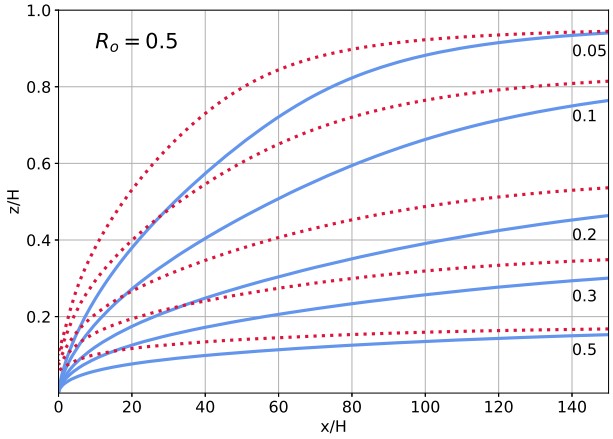

Figure 10. Isolines of c_s/c_b^*. Comparison between pseudo-analytical solution from Hjelmfelt and Lenau (1970) (red dotted lines) and the model solution (solid blue lines) without enforcement of the hypothesis used to derive the pseudo-analytical solution.

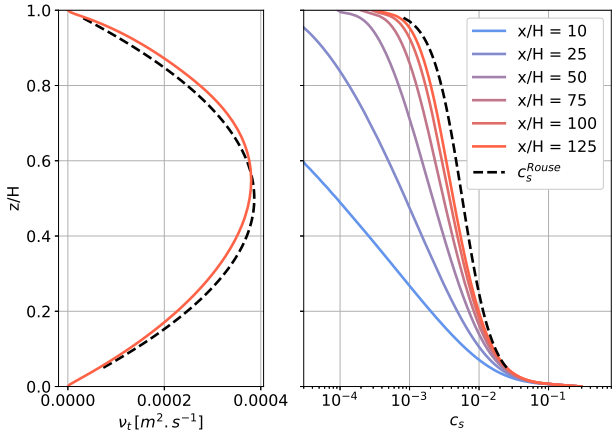

Figure 11. On the left hand side, the turbulent eddy viscosity obtained with the model (solid line) and the theoretical parabolic profile (black dashed line). On the right hand side, vertical profiles of c_s at different x-positions in the channel. For comparison, the Rouse profile corresponding to the pseudo analytical solution in Figure 10 is also plotted (black dashed line).

ν_t profile. Another adjustment parameter is the reference concentration at the reference level which is the bottom boundary condition of the pseudo analytical solution.

These suspension development simulations require 10 hours of wall-clock time on 5 CPU cores to compute 50 seconds of physical simulation time.

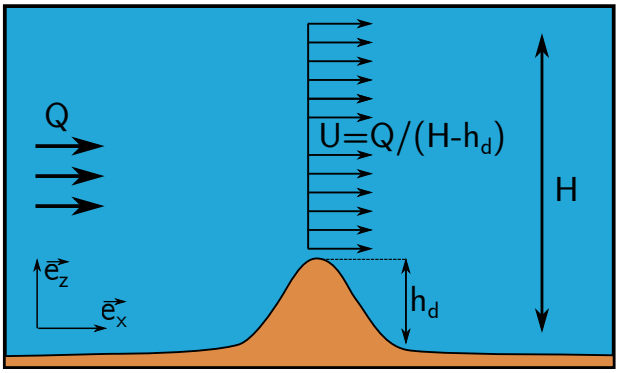

Figure 12. Schematic of the idealized dune transport case.

4.3 Idealized dune transport

As a first benchmark for the Exner equation (Eq. 11), an idealized 1D dune transport model for which an analytical solution exists is presented. In this case, a highly simplified flow is considered in order to focus on the behavior of the Exner equation without the added complexity of the hydrodynamics (see Figure 12). The fluid is topped by a rigid lid placed at an elevation H from the bottom. The flow is considered vertically uniform with a constant discharge per unit width Q. The depth-averaged velocity is obtained by conservation of the mass, $U = Q/(H - z_b)$.

In this simplified case, only bedload transport is considered. To be able to derive an analytical solution of the Exner equation, the bedload q_b must be expressed as a function of the bed elevation z_b. This is done by assuming that the bedload is a power law of the depth-averaged velocity U, $q_b = \alpha_d U^{\beta_d}$, where α_d and β_d are two positive constants. The Exner equation (Eq. 11) simplifies to:

$$\frac{\partial z_b}{\partial t} + c(z_b)\frac{\partial z_b}{\partial x} = 0\,, \tag{29}$$

$$c(z_b) = \frac{\partial q_b}{\partial z_b} = \frac{\alpha_d \beta_d Q^{\beta_d}}{(H - z_b)^{\beta_d + 1}}\,, \tag{30}$$

where $c(z_b)$, is the celerity of the bed form. Starting with a given initial bedform $z_b(x, t = 0) = F_0(x)$, the solution to equation 29 is obtained with the method of characteristics (McOwen, 1996) leading to $z_b(x, t) = F_0(x - ct)$. Depending on F_0, shocks may develop as the bedform migrates. A shock occurs if, over at least one interval $\mathcal{I} \in \mathbb{R}$, the function $G : x \to c(F_0(x))$ is decreasing. The dune celerity c being an increasing function of z_b, shocks will arise if the initial bedform F_0 exhibits at least one negative slope. In this idealized dune transport case the initial dune profile is Gaussian:

$$F_0(x, t) = h_d\, e^{-\left(\frac{x - x_d^0}{\sigma_d}\right)^2}\,, \tag{31}$$

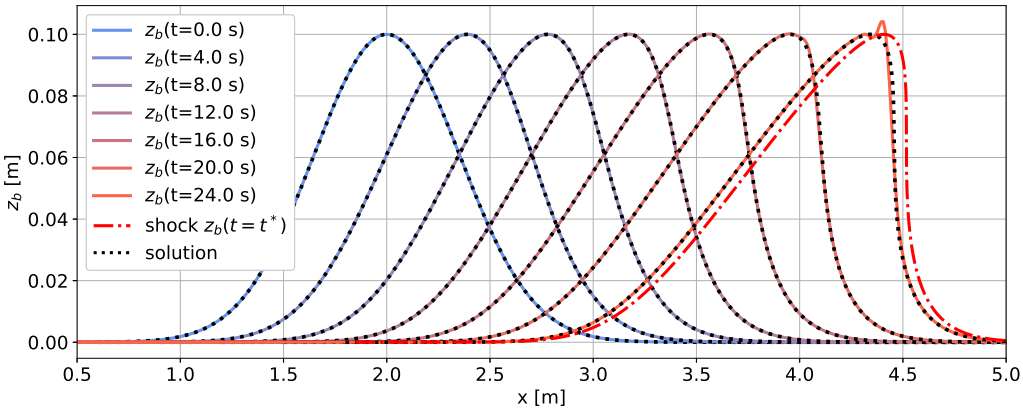

Figure 13. Dune transport problem, comparison between model results (solid lines) and analytical solution (black dotted lines) at different times.

with h_d the height of the dune, x_d^0 the initial position of the top of the dune and σ_d a parameter linked to the dune width such that $F_0(x_d \pm \sqrt{\ln(2)}\sigma_d) = 0.5 h_d$.

With this initial dune profile, a shock wave will form where the bed slope becomes vertical on the lee side of the dune. In order to know the position and time of the shock, it is needed to find the position x_0^* defined as follows, $G'(x_0^*) = min_{x \in \mathcal{R}}\,(G(x))$. It corresponds to the initial position of the point belonging to the caracteristic line on which the first shock occurs. The breaking time is then obtained as $t^* = -1/G'(x_0^*)$ and the shock position x^* as well by advection of x_0^* along its characteristic line, $x^* = x_0^* + G(x_0^*)t^*$.

The following parameters are chosen:

- flow properties, $H = 1\,\mathrm{m}$ and $Q = 1\,\mathrm{m}^2.\mathrm{s}^{-1}$
- bedload flux, $\alpha_d = 0.05$ and $\beta_d = 1.5$
- dune properties, $h_d = 0.1\,m$, $\sigma_d = 0.6\,\mathrm{m}$

For this configuration, the breaking time is $t^* = 24.67\,\mathrm{s}$ and the shock position $x^* = 4.51\,\mathrm{m}$. A solution to equation 29 is sought for the time interval between $t = 0$ and the breaking time t^*. A second order *Adams-Bashforth* scheme is used for time discretization and a *linear-upwind* scheme for the advective term. A comparison between the model results and the analytical solution is presented in Figure 13. Overall, the model fits well with the analytical solution except when the time gets close to the breaking time where a small instability is starting to develop at the dune's crest. Figure 14 illustrates how the chosen numerical schemes affect the solution stability and precision.

At the dune front, the gradient of z_b becomes important and consequently the gradient of q_b as well. Depending on the numerical schemes used, this can trigger oscillations. Using the *Euler explicit* scheme for time discretization, the use of a second order scheme for advection leads to instabilities appearing on the crest of the dune. On the other hand, the low order

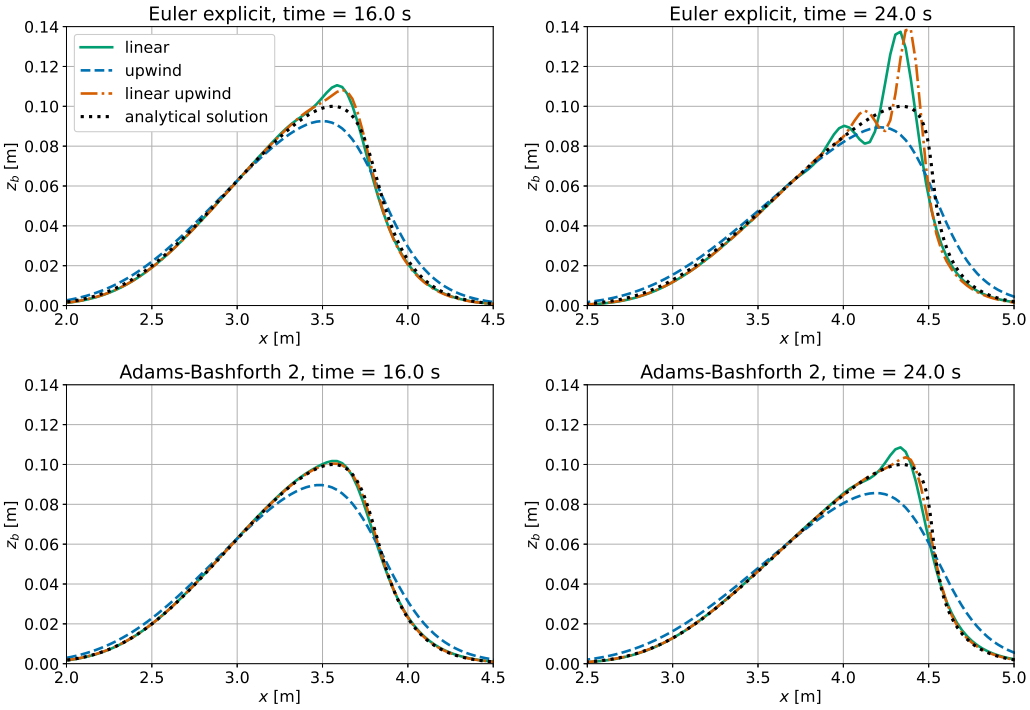

Figure 14. Comparison of results obtained with the three different numerical schemes for the advective term and the two schemes for temporal discretization (*Euler explicit* on top plots and *Adams-Bashforth 2* on bottom plots). The comparison is made at two different times, one intermediate time (left plots) and one time close to the breaking time (right plots).

upwind scheme brings up numerical diffusion and thus a poor prediction but ensures numerical stability. A better match between the numerical results and the analytical solution is achieved using a second order scheme for the temporal term (*Adams-Bashforth 2*) as the numerical solution no longer oscillates.

As stated in section 3.2, the interpolation from faces to vertices needed to enforce mesh motion acts as a filter, however, depending on the case, it may not be sufficient to suppress the appearance of numerical instabilities in particular in regions presenting steep slopes. The use of an avalanche model (Eq. 14) brings more stability by limiting the maximum bed slopes. However it is not used in this example as no analytical solution can be derived for this problem if the avalanche mechanism is taken into account.

From the results presented in Figure 14, the combination of a second order *Adams-Bashforth* scheme for the time discretization and a *linear* or *linear-upwind* scheme for the bedload flux, both being second order schemes, seems to offer the best compromise between stability and accuracy. Choosing an *Euler explicit* time scheme tends to trigger instabilities while the use of an order 1 *upwind* scheme leads to more stability at the cost of accuracy. To further illustrate the different behaviors of the possible scheme combinations and for different mesh refinements, multiple simulations are performed by varying the grid size and the numerical schemes, and the results are compared with the analytical solution.

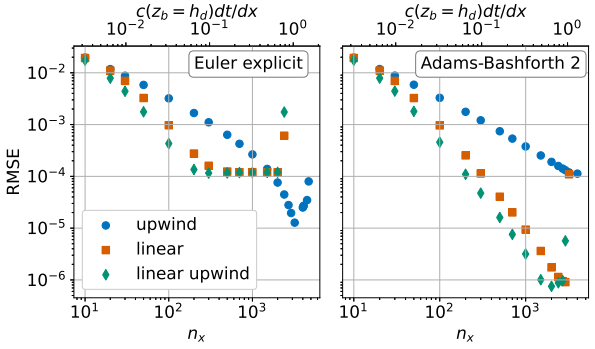

Figure 15. Root Mean Square Error for different combinations of schemes and mesh refinements. The time step is constant $\delta t = 0.05\,\mathrm{s}$ for all simulations.

The stability of the numerical solution is related to the mesh refinement through the maximum Courant number, whose evaluation is straightforward as the celerity of bedforms c is known (Eq. 29). The maximum Courant number is then $\max(C_o) = c(z_b = h_d)\delta t/\delta x$ where δt is the time step value and δx the width of the mesh faces in the x-direction, the mesh being uniform. The accuracy of the numerical solution is evaluated using the Root Mean Square Error (RMSE):

$$\mathrm{RMSE} = \sqrt{\frac{1}{N_F}\sum_f (z_b^n|_f - z_b^s|_f)^2}\,, \tag{32}$$

where the index f stands for the finite area mesh faces, N_F the number of faces of the mesh, z_b^n is the elevation of face f center (numerical solution) and $z_b^s|_f$ is the analytical bed elevation at face f center. Each simulation is represented by a point in Figure 15.

The simulations were performed using a constant time step. For low Courant numbers, associated with poor mesh quality, all simulations remain stable and exhibit similar errors. As the mesh quality increases, the RMSE decreases but at a faster rate for second order schemes for bedload advection until the solution becomes unstable when the maximum Courant number gets close to 1. The sudden rise of RMSE values for high mesh resolution is the sign of those instabilities. The use of an *upwind* scheme allows to use an higher Courant number without the simulation failing. This is due to the numerical diffusion that this first order scheme involves. When using an *Euler explicit* time scheme along with one of the second order schemes for advection, it is observed that the RMSE does not depends anymore on the mesh resolution for values of maximum Courant number of 0.1 and higher until the appearance of instabilities. It shall be recalled here that a filtering process is applied on the numerical solution at each time step as the bed elevation increment is interpolated from faces to vertices (discussed in section 3.2). The results presented support the use of a combination of a second order *Adams-Bashforth* scheme along with a *linear* or *linear-upwind* scheme to ensure both stability and accuracy.

These simulations complete in a few seconds on a single CPU core.

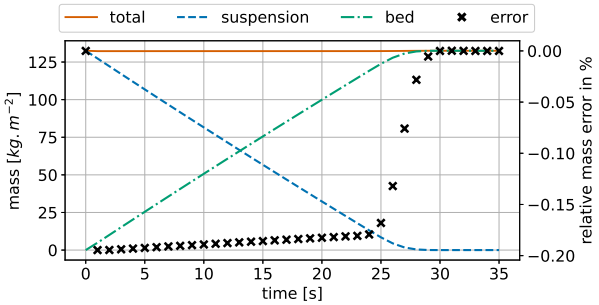

Figure 16. Variation over time of the sediment mass per unit area divided into suspended and deposited sediments. The relative error on the total mass in percentage is represented by black crosses.

4.4 Sediment settling

A still basin of depth $H = 1\,\mathrm{m}$ is initially uniformly loaded with a volume fraction $c_s^0 = 0.05$ of suspended sediment corresponding to a mass concentration of $132\,\mathrm{kg.m^{-3}}$. As the suspended sediment deposit, the bed level rises up and reaches a final elevation $z_{bed} = \frac{c_s^0}{1-\lambda_s} H$, where λ_s is the porosity of the deposited granular material. The settling velocity being set to $w_s = 3.59\,\mathrm{cm.s^{-1}}$, the time at which the last sediment deposit on the bed is $t = \frac{H - z_{bed}}{w_s}$. The variation over time of the sediment mass distribution between suspension and deposited sediments is represented in Figure 16.

During each time iteration, the equation for the concentration of suspended sediments is solved, and the erosion/deposition flux is computed, resulting in an updated sediment bed elevation via the Exner equation (see Figure 5). Since the mesh motion is resolved at the beginning of the time iteration, the bed level increment computed at a given step only affects the mesh geometry in the subsequent time step. Consequently, there is a one-time-step delay in the morphological response of the bed, which introduces a temporary error in the total sediment mass. However, this error vanishes once all suspended sediments have settled.

Another settling case is presented, this time a 2D case with non uniform settling. The computational domain is conic shaped, wider at the bottom (5cm) and narrower at the top (1cm). Initially, only water is present in the domain and sediments are injected at the top boundary condition with a constant concentration. The sediments settle under the action of gravity and deposit on the bed. Because the settling is not spatially uniform, pronounced slopes form at the margins of the deposition mound, where avalanching occurs, producing a conical shape similar to that seen in an hourglass. The repose angle is taken equal to $\beta_r = 32°$. The sediments diameter is $d = 0.29\,\mathrm{mm}$ and their density $\rho_s = 2600\,\mathrm{kg.m^{-3}}$. The sediment settling velocity $w_s^0 = 3.5\,\mathrm{cm.s^{-1}}$ is computed using the formula from Fredsoe and Deigaard (1992) (see Table 1) and is considered uniform as the hindrance effect is not taken into account. A constant flux of sediment is injected during 7 seconds by imposing a constant suspended sediment volume fraction at the top boundary $c_s = 0.05$. The simulation then run for 3 more seconds so that all sediments have settled by the end of the simulation (see Figure 17).

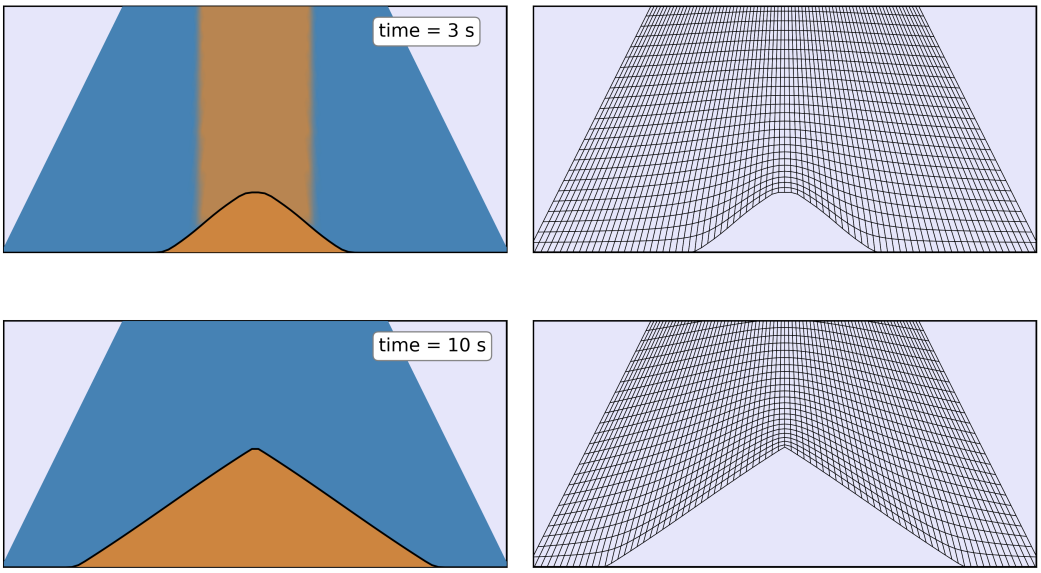

Figure 17. Representation of the sediment in the domain at two different times. At 3 seconds where a deposition mound is being formed as suspended sediment deposit and 10 seconds where all the sediments have settled. On the left, the colors indicate the presence of water (blue) and sediment (orange). The corresponding mesh is shown on the right.

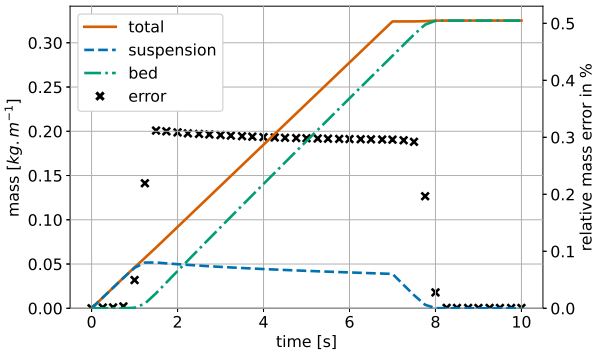

Figure 18. Variation over time of the sediment mass per unit area divided into suspended and deposited sediments. The relative error on the total mass in percentage is represented by black crosses. Suspended sediments is injected during the 7 first seconds and all deposit before the simulation end.

The mass repartition of sediments between suspension and deposition is represented in Figure 18. At the beginning of the simulation, all the sediments are suspended and their quantity increases linearly over time until $t = 1.14\text{s}$ where the sediments

start depositing on the bed. As the domain bottom boundary rises, the space occupied by suspended sediments shrinks leading to a diminution of the mass of suspended sediments. At 7 seconds, sediments stop being injected into the domain and approximately one second later, all the sediment have settled. Once again the mass error is evaluated by comparing the mass of sediment which has been injected into the domain to the sum of the suspended mass and the bed mass. Just as in the 1D case, the one time step delay in the bed morphology response induces an error on the total mass in the domain (see Figure 18). This error then vanishes as the sediments settle so that the mass conservation is verified.

These simulations complete in a few seconds on a single CPU core.

5 Application to dune transport

Sediment transport phenomena often involve bedforms of various scales, ranging from ripples to megadunes, which migrate under the influence of fluid flow. Building on the validation of the model components presented in Section 4, this section examines the transport of an isolated dune under a steady current as an illustrative application of sedExnerFoam. First, the experiment used for model comparison is presented, followed by a description of a source term introduced to account for lateral wall friction. The numerical simulation of a dune in a stationary migration regime is presented, where incorporating bedload saturation was necessary to reproduce the migration behavior observed in the experiments. The effects of other model parameters on the simulation results are also briefly discussed.

5.1 Configuration

The subject was studied experimentally by Kiki Sandoungout (2019) as he tried to identify different regimes of dune propagation and the dependence of those regimes to the flow conditions and to the dune mass. In this case study, the focus is made on one specific regime observed by Kiki Sandoungout and called the stationary regime. Two stages are observed, during the first one, the dune morphology rapidly changes from an initial conic shape obtained by deposition of sediments in still water. After the initial transient phase over which the bed porosity evolves, the dune reaches a stationary state and moves at a constant velocity in the flow direction.

The experimental facility consists of an hydraulic tunnel working in closed circuit with an experimental area made of a straight channel of length $L_c = 900\,\mathrm{mm}$, of height $H_c = 90\,\mathrm{mm}$ and of thickness $W_c = 6.03\,\mathrm{mm}$. The flume is closed on the top by a rigid lid and is entirely filled with water. The granular material is made of glass beads of high sphericity. Their diameter is $d = 0.4\,\mathrm{mm}$ and density $\rho_s = 2500\,\mathrm{kg.m^{-3}}$. The particles terminal fall velocity in water is $w_s^0 = 7.67\,\mathrm{cm.s^{-1}}$ which is noticeably higher than values obtained with the models presented in Table 2 ($w_s^0 \approx 5\,\mathrm{cm.s^{-1}}$). The friction velocity upstream of the dune is $u_* = 2.78\,\mathrm{cm.s^{-1}}$ which corresponds to a Rouse number $R_o = 6.73$. This value indicates that bedload is the main transport mechanism for this problem. The critical Shields number ($\theta_c^0 = 0.079$) obtained experimentally is large compare to what is expected from the formulas in Table 2. This could be due to the confinement of the particles in the flume, the ratio of the channel width to the particle diameter being only equal to 16.

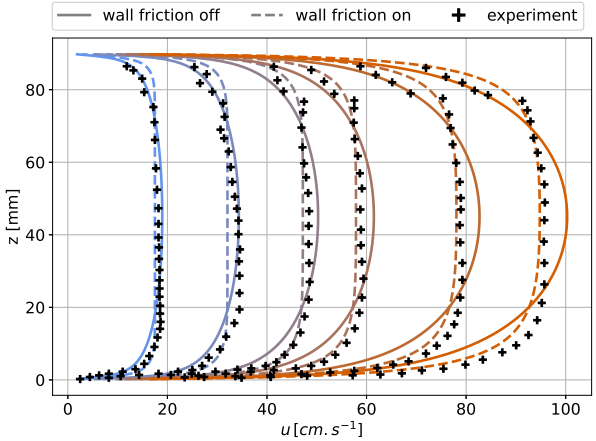

Figure 19. Velocity profiles obtained for different bulk velocities ($0.169\,\mathrm{m.s^{-1}}$, $0.309\,\mathrm{m.s^{-1}}$, $0.451\,\mathrm{m.s^{-1}}$, $0.549\,\mathrm{m.s^{-1}}$ and $0.732\,\mathrm{m.s^{-1}}$). The solid lines represent profiles obtained without friction on the lateral walls and the dashed line to the one obtained taking into account the lateral friction. The markers are experimental results from Kiki Sandoungout (2019).

An important aspect of this experiment is the thinness of the flume which makes the lateral wall friction not negligible. The lateral variation of the flow is neglected and the specific shear stress on the lateral walls $\boldsymbol{\tau_{wall}}$ is computed with the Darcy-Weissbach equation:

$$\boldsymbol{\tau_{wall}} = \rho_f f \frac{|\boldsymbol{u}|\boldsymbol{u}}{8}, \tag{33}$$

where f is the Darcy-Weissbach friction factor which can be computed explicitly with the equation from Swamee and Jain (1976):

$$f = \frac{0.25}{\left[\log_{10}\left(\frac{k_w/D_h}{3.7} - \frac{5.74}{Re_W^{0.9}}\right)\right]^2}, \tag{34}$$

where $D_h = 2H_cW_c/(H_c+W_c)$ is the hydraulic diameter, k_w the roughness height corresponding to the roughness of the wall and $Re_W = |\boldsymbol{u}|D_h/\nu$ is the Reynolds number defined with the flume width. Integrating the momentum conservation equation (Eq. 1) over the flume width, a new source term $\boldsymbol{F_{walls}}$ corresponding to the effect of the lateral wall appears:

$$\boldsymbol{F_{walls}} = -f\frac{|\boldsymbol{u}|\boldsymbol{u}}{4W_c}. \tag{35}$$

More detail on the derivation of this source term are provided in Appendix B.

In order to confirm the capability of the wall friction term to correctly predict the flow velocity in the narrow flume, five simulations corresponding to different discharges as reported in the experiments are performed. Figure 19 shows a summary of these runs with and without the lateral friction term. Lateral friction leads to a more uniform velocity field as the distance to the upper and lower walls increases, as well as to higher velocity gradients near the boundaries. The agreement with experimental

data is improved except at the top of the domain where the flow is disturbed by the presence of a screw hole, which makes the data noisy and unreliable in this area. The main advantage of taking into account lateral friction as a source term is that it enables the use of a 2D mesh, which significantly reduces the computational cost of the simulation.

A stationary regime configuration is reproduced numerically. A mass $m_0 = 10\,\mathrm{g}$ of sediment is introduced through a hole drilled in the channel cover. It deposits under the influence of gravity and form a conic shaped mound with slope angles equal to the angle of repose of the granular material. Once the initial pile has formed, a motor is activated to create a left-to-right flow in the experimental zone with a bulk velocity $\overline{u} = 0.43\,\mathrm{m.s}^{-1}$. Initially the sediments are loosely packed with a volume fraction of $c_s^{\max} \approx 0.54$ in the bed. As the dune is transported by the flow the sediments get compacted and the sediment volume fraction in the bed increases resulting in the dune volume decreasing over time until the volume fraction reaches a constant value $c_s^{\max} \approx 0.6$. This variation of the sediment volume fraction in the bed cannot be reproduced by the present model in which the bed porosity is considered constant over space and time. Therefore, it was chosen to initialize the dune with a volume corresponding to the one at the end of the experiment and not the initial one. As a result, the numerical dune is initially smaller than the experimental one but their volumes match after some time, once the granular material has compacted.

Regarding the boundary conditions, a uniform velocity is applied at the inlet $\overline{u} = 0.43\,m.s^{-1}$ and it was verified through a sensitivity analysis to the upstream domain length that the solution does not change when using a longer domain. Dirichlet conditions are also used at the inlet for the turbulent quantities, respectively $k = 0.001\,m^2.s^{-2}$ and $\omega = 15\,s^{-1}$ at the inlet boundary. It corresponds to a turbulent intensity $I_t = \sqrt{\frac{2}{3}k}/\overline{u} = 0.06$. Those values were chosen after simulating the flow in the flume without sediments and it was ensured that the length upstream of the dune was sufficient for the flow to fully develop. The top boundary is a rigid wall and a no slip boundary condition is thus applied on the velocity field. At the outlet, a zero gradient condition is applied to all field except the pressure for which a Dirichlet condition is used.

Experimentally, the fluid is initially still and the pump starts to operate at $t = 0\,s$ accelerating the flow to the selected velocity setpoint. As the time it takes for the flow to accelerate and reach a mean velocity $\overline{u} = 0.43\,m.s^{-1}$ is unknown, it was chosen to initialize the problem differently. A first simulation of the hydrodynamics without morphological evolution runs for 10 seconds until the flow over the dune reaches a steady state. The morphological evolution is then activated and the dune begins to move under the influence of an already fully developed flow. The results are illustrated in Figure 20 which represent the dune and the flow of water at three different times.

This inconsistency in the initial condition leads to a different morphological response in the first few seconds of the simulation. The different adjustment parameters of the model were thus tuned to match the experimental results beyond the first 5 seconds of simulation. As seen in Figure 21, the numerical and experimental dunes are not matching the experiment during the first few seconds but as they approach a stationary regime their shape and velocity start to align satisfactorily.

The results presented in Figures 21 and 22 were obtained after multiple simulation attempts and a sensitivity analysis of the various model parameters. A first element that significantly affects the results is the resolution of the mesh and in particular the near bed resolution in the areas where the flow is highly non uniform. In this case study, it corresponds to the upstream slope of the dune where the flow is contracted and accelerated until the top of the dune where the flow detaches and generates a recirculation cell illustrated in Figure 20. A poor near bed mesh quality leads to an under estimate of the bed shear stress and

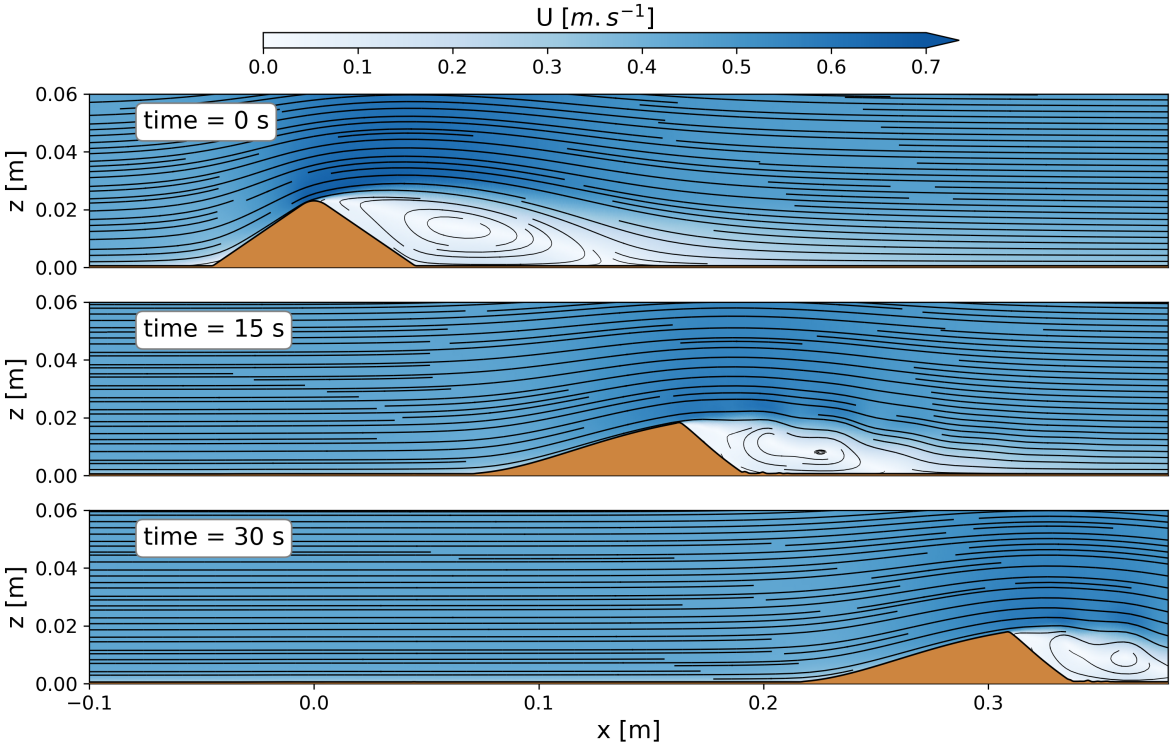

Figure 20. Representation of the dune and the flow streamlines at different times during the migration process.

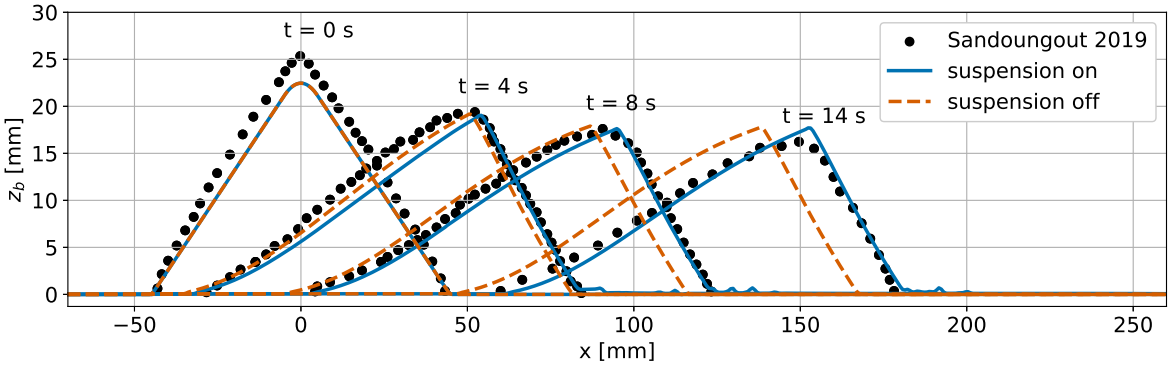

Figure 21. Sediment bed elevation at different times, 0, 4, 8 and 14 seconds. Comparison between results from two simulations and experimental results. The simulations use the same mesh, same parameters but for one, the suspended load is not taken into account.

as a consequence to a slower dune migration. The distance in wall unit between the cell centers making up the first layer of cells above the bed boundary and the bed boundary is kept between $z^+ = 1$ and $z^+ = 5$. Not surprisingly the numerical scheme used to discretize the advective term in the momentum equation (Eq. 1) was also found to affect the dune shape. This is mainly

because of its effect on the recirculation cell caracteristics and the position of the detachment region which is located upstream of the dune crest with high order schemes but downstream with a low order *upwind* scheme. When the flow detachment appears downstream of the dune crest, the dune shape was found to take a rounder shape not matching the experiment. A second order *linear-upwind* scheme was used to produce the results presented.

Another parameter of importance in this case is the critical Shields number θ_c^0 which is evaluated in the range $0.033 - 0.046$ by the different models presented in Table 2 but was experimentally estimated at a higher value of 0.079. Increasing the value of θ_c^0 not only slows down the dune but also reduces its height and length in the stationary regime. An intermediate value of $\theta_c^0 = 0.05$ was found to yield good results. In addition, the critical Shields number was corrected with the local slope according to equation 12. A last key parameter is the formula chosen to calculate the bedload transport. It was found that the formulas presented in Table 2 were all predicting dune velocity at least two times slower than the one observed experimentally. Therefore, a custom bedload formula $\phi_b = 32\theta^{1/2}\varpi(\theta - \theta_c)$ was used. It corresponds to an intensified version of the formula from Nielsen (1992) and can be considered reasonable in view of the significant scatter associated to bedload measurements (Recking, 2010). Indeed, even if these formulations are commonly used to model sediment transport in a variety of flow conditions, they are empirical relations derived from data of uniform flows in a straight channel. Therefore, they may not precisely describe sediment transport in accelerated flow regions, recirculation cells and other non uniform flows features.

A last critical point is the inertia of the sediments. On the upstream slope of the dune, the flow is accelerated and the bed shear stress increases. At the position where the flow detaches, the shear stress value suddenly drops. If the inertia of the bedload is not taken into account, then the sediments accumulate at the crest and the dune height increases. At some points the upstream slope becomes steeper than the angle of repose and the avalanche bedload compensates the shear induced bedload. The dune then stops moving and stays stuck in a non physical state. In reality, the sediments arrive at the crest with a certain velocity and some distance is needed for them to react to the sudden change of the bed shear stress. They could even be launched into suspension due to the abrupt change of slope at the crest of the dune. To retrieve a behavior of the dune migration similar to the experiment, it was found necessary to consider the sediments inertia which is done at first order by using the saturation of the bedload flux (Eq. 15). The results presented in this work have been obtained using a saturation length $L_{sat} = 5\,\mathrm{mm}$ and no saturation in time was considered.

The dune morphological parameters over time which are the dune position, its height and length are represented in Figure 22. The dune position is represented by the coordinate x_h located at mid-height on the downstream slope of the dune. The dune height and length are estimated from the base of the triangle formed by two straight lines fitted on the dune upstream and downstream slopes (see Appendix C). Two simulations with and without considering the suspended load transport are represented. As expected because of the high value of the Rouse number ($R_o > 6$), the suspension is having little effect on the dune evolution. Its height and length in the stationary regime remain unchanged and regarding the migration velocity only a small difference is observed, $9.88\,\mathrm{mm.s^{-1}}$ and $8.75\,\mathrm{mm.s^{-1}}$ for simulations with and without considering the suspended load respectively. This velocity difference is also observed in Figure 21 showing the bed elevation profiles at different times. n the case with suspended load, part of the suspended sediment passes over the dune and settles within the recirculation zone, creating the artifacts observed downstream. These deposits are subsequently re-assimilated by the dune as it migrates.

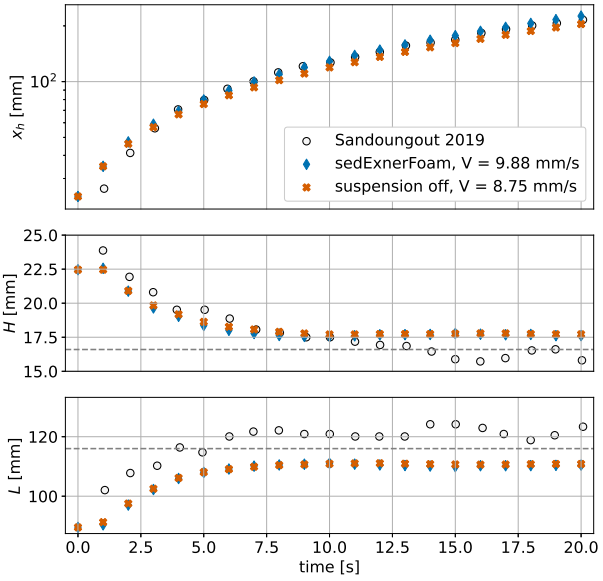

Figure 22. Dune morphological parameters evolution in time. From top to bottom are plotted the dune position represented by the coordinates x_h, which is located halfway up the downstream face of the dune, as well as the dune height and the dune length.

Overall the numerical model is able to reproduce the dune migration and evolution correctly, but some discrepancies are still observed. The crest of the dune is sharp in both numerical simulations compared to the experience and as a result, the height of the dune is slightly overestimated (see Figure 22). At the same time, the length of the dune seems to be underestimated but it could also be a consequence of the method used to estimate the dune length (see Appendix C). The two stages of the dune migration are clearly observed. During the first 10 seconds, the dune shape changes rapidly, its height decreases and its length increases. At 10 seconds, the dune has reached a stationary stage and its shape remains unchanged as it migrates at a constant velocity.

Regarding computational cost, the current implementation requires approximately 30 minutes of wall-clock time on a single CPU core to simulate 10 seconds of morphodynamics without saturation. When saturation is activated, the non-optimized implementation slows the computation, increasing the cost to about 45 minutes for the same simulated duration.

6 Conclusions

A new numerical code, *sedExnerFoam*, aimed at studying sediment transport and the evolution of morphology, is proposed. Developed within *OpenFOAM*® (v2412), it is based on the *pimpleFoam* solver. Numerous closures for the settling velocity of particles, the bedload flux and the critical Shields number are implemented and can be modified by the user, thanks to the object-oriented environment offered by *OpenFOAM*.

The model has been extensively validated using multiple tests against analytical solutions or experimental data, covering a wide range of applications from turbulent suspension in open-channel flows to idealized dune transport, sand deposition, and mass conservation in an hourglass. These benchmarks were selected to isolate and test each component of the model individually. Lastly, applying the model to the migration of a lone dune under the influence of a steady flow illustrates its capability to handle complex problems. This process involves flow detachment, avalanching and is associated with significant mesh deformation. It was also found that the inertia of sediments transported as bedload was essential in describing sediment fluxes at the crest of the dune, in order to match the observed morphological evolution in experiments. The inertial effects of the particles are introduced as a saturation or adaptation length for the bedload flux with respect to the fluid bed shear stress. As the position of the flow detachment point is particularly important, the turbulence model and the numerical scheme used to discretize the advection term in the fluid momentum equation must be chosen carefully. These choices can significantly affect the flow separation and the underlying morphodynamics. It was also found that the inertia of the sediments transported as bedload is essential for describing the sediment fluxes at the crest of the dune in order to match the morphological evolution observed in experiments.

The model's main strengths are its open-source availability and extensive validation on idealized benchmarks. From a software development perspective, using continuous integration tests on the GitHub repository helps to ensure the long-term maintenance of the code, as well as backward compatibility over time. Using the proposed avalanche model eliminates the need for the costly and unphysical iterative procedure employed in most existing 3D morphological models. Another novel feature introduced in this work is the near-wall diffusivity for turbulent suspensions, which enables the use of the same mesh for flow hydrodynamics and sediment concentration. To the authors' knowledge, the application of bedload flux saturation is unique to this subaqueous sediment transport numerical model, and is essential for accurately predicting dune migration.

Beyond possible future developments, such as the addition of a free surface, accounting for multiple grain sizes or modeling cohesive sediments, the following limitations have been identified: (i) the feedback of the suspended sediment concentration on the flow hydrodynamics (e.g. through a Boussinesq term); (ii) the mesh resolution required for the accurate estimation of bed shear stress in regions of non-uniform flow, including bed roughness; (iii) the mesh deformation solver, which may cause the simulation to crash; (iv) the development, validation and implementation of filters for bed evolution; and (v) the formulation, implementation and validation of a multi-dimensional bedload flux saturation model.

In the long term, *sedExnerFoam* is planned to be used alongside *sedFoam* (Chauchat et al., 2017), a two-phase flow model for sediment transport, to derive more accurate and robust closures for sediment transport fluxes through an upscaling process.

Code and data availability. *sedExnerFoam* Renaud et al. (2025) model code, associated libraries, tests and tutorials are all available via zenodo at https://doi.org/10.5281/zenodo.15535485 or directly via GitHub at https://github.com/SedFoam/sedExnerFoam. Instructions for installation and explanations on the repository organization are provided in a README file.

Author contributions. JC, CB, and OB designed the project. MR developed the source code, ran simulations, and wrote the paper. JC edited the manuscript. Supervision: CB, OB, JC. All authors discussed the results and contributed to the final paper.

Competing interests. The contact author has declared that none of the authors has any competing interests.

Abbreviations and Notations

Abbreviations

ALE	Arbitrary Lagrangian Eulerian
CFD	Computational Fluid Dynamics
DNS	Direct Numerical Simulation
FAM	Finite Area Method
FVM	Finite Volume Method
IBM	Immersed Boundary Method
LES	Large Eddy Simulation
RAS	Reynolds-Averaged Simulation
RMSE	Root Mean Square Error
SMAPE	Symmetric Mean Absolute Percentage Error
SST	Shear Stress Transport
TKE	Turbulent Kinetic Energy

Notations

c_s	Suspended sediment volume fraction
c_s^{max}	Maximum sediment volume fraction
c_b^*	Reference concentration
$c_{b,max}^*$	Maximum reference concentration
C_D	Drag coefficient
d	Diameter of the sediment $[\mathrm{m}]$
D	Deposition rate $[\mathrm{m.s}^{-1}]$

	D_h	Hydraulic diameter, 4 times the ratio of the wet area to the wet perimeter $[\mathrm{m}]$
	D_*	Dimensionless sediment diameter
	E	Erosion rate $[\mathrm{m.s^{-1}}]$
	f	Darcy-Weissback friction factor
	F_h	Hindrance function
	$\boldsymbol{F_{walls}}$	Side walls friction source term $[\mathrm{m.s^{-2}}]$
	F_1	First blending function of the $k-\omega\,SST$ model
	F_2	Second blending function of the $k-\omega\,SST$ model
	F_3	Third blending function of the $k-\omega\,SST$ model
	$\boldsymbol{g}$	Gravity acceleration $[\mathrm{m.s^{-2}}]$
	k	Specific turbulent kinetic energy $[\mathrm{m^2.s^{-2}}]$
	k_s	Nikuradse equivalent roughness height $[\mathrm{m}]$
	k_s^+	Roughness Reynolds number
	k_w	Wall equivalent roughness height $[\mathrm{m}]$
	L_{sat}	Saturation length $[\mathrm{m}]$
	l_{sb}	Distance to the sediment bed boundary $[\mathrm{m}]$
	p	Pressure of the fluid $[\mathrm{kg.m^{-1}.s^{-2}}]$
	P	Specific turbulent kinetic energy production rate $[m^2.s^{-3}]$
	$\boldsymbol{q_{av}}$	Avalanche related bedload flux $[\mathrm{m^2.s^{-1}}]$
	q_{av}^0	Maximum avalanche related bedload flux $[\mathrm{m^2.s^{-1}}]$
	$\boldsymbol{q_b}$	Bedload flux $[\mathrm{m^2.s^{-1}}]$
	$\boldsymbol{q_{sat}}$	Saturated bedload flux $[\mathrm{m^2.s^{-1}}]$
	R_o	Rouse number, ratio of the settling velocity to the upwards velocity of the grains
	s	Ratio of sediment density to fluid density
	$\boldsymbol{S}$	Strain rate tensor $[\mathrm{s^{-1}}]$
	S_R	Roughness coefficient in rough wall functions for ω
	t^*	Breaking time $[\mathrm{s}]$
	T_{sat}	Saturation time $[\mathrm{s}]$
	$\boldsymbol{u}$	Fluid velocity field $[\mathrm{m.s^{-1}}]$
	$\boldsymbol{u'}$	Fluctuating velocity field $[\mathrm{m.s^{-1}}]$

	u_*	Friction velocity $[\mathrm{m.s^{-1}}]$
835	V_f	Volume of fluid $[\mathrm{m^3}]$
	V_s	Volume of sediments $[\mathrm{m^3}]$
	$\boldsymbol{w_s}$	Settling velocity of suspended sediment $[\mathrm{m.s^{-1}}]$
	w_s^0	Terminal settling velocity of a lone particle in a quiescent fluid $[\mathrm{m.s^{-1}}]$
	z_b	Sediment bed elevation $[\mathrm{m}]$
840	α_s	Angle between the steepest slope direction and the shear direction
	β_r	Repose angle of the granular material
	β_s	Bed slope angle
	Γ_c	Mesh diffusivity $[\mathrm{m^2}]$
	δz_b	Bed elevation increment $[\mathrm{m}]$
845	δz_b^*	Reference level $[\mathrm{m}]$
	$\boldsymbol{\Delta X_c}$	Cell center displacements $[\mathrm{m}]$
	ϵ	Dissipation rate of turbulent kinetic energy $[\mathrm{m^2.s^{-3}}]$
	ϵ_s	Turbulent diffusivity for suspended sediment $[\mathrm{m^2.s^{-1}}]$
	ϵ_w	Additional near bed diffusivity for suspended sediment $[\mathrm{m^2.s^{-1}}]$
850	ϵ_w^0	Constant in the near bed diffusivity definition
	θ	Shields number, dimensionless bed shear stress
	θ_c^0	Critical Shields number on a flat bed
	θ_c	Critical Shields number with slope correction
	κ	Von Kármán constant
855	λ_s	Porosity of the granular material
	μ_s	Static friction coefficient
	ν	Kinematic viscosity of the fluid $[\mathrm{m^2.s^{-1}}]$
	ν_t	Turbulent eddy viscosity $[\mathrm{m^2.s^{-1}}]$
	ξ_w	Constant in the near bed diffusivity definition
860	ρ_f	Density of the fluid $[\mathrm{kg.m^{-3}}]$
	ρ_s	Density of the sediment $[\mathrm{kg.m^{-3}}]$
	σ_c	Schmidt number, ratio of eddy viscosity to turbulent diffusivity of suspended sediments
	$\boldsymbol{\tau_b}$	Shear stress exerted on the bed $[\mathrm{kg.m^{-1}.s^{-2}}]$

$\boldsymbol{\tau_f}$ Filtering tensor in Navier-Stokes equation [$\mathrm{m}^2.\mathrm{s}^{-2}$]

$\boldsymbol{\tau_{wall}}$ Lateral wall friction [$\mathrm{kg}.\mathrm{m}^{-1}.\mathrm{s}^{-2}$]

ϕ_b Dimensionless bedload flux

ω Specific dissipation rate of turbulent kinetic energy [s^{-1}]

Appendix A: RANS $k-\omega$ SST model

The blending function F_1 is defined as follows:

$$F_1 = \tanh\left[\min\left(\min\left(\max\left(\frac{\sqrt{k}}{\beta_* \omega y}, \frac{500\nu}{\omega y^2}\right), \frac{4\alpha_{\omega 2} k}{CD^+_{k\omega} y^2}\right), 10\right)^4\right], \tag{A1}$$

$CD^+_{k\omega}$ stands for the positive portion of the cross-diffusion term and is defined as:

$$CD^+_{k\omega} = \max\left(2\alpha_{\omega 2} \nabla k . \frac{\nabla \omega}{\omega}, 10^{-10}\right). \tag{A2}$$

The blending function appearing in the eddy viscosity definition (eq. 3) is defined as $F_{23} = F_2 F_3$ where F_2 is defined as follows:

$$F_2 = \tanh\left[\min\left(\max\left(\frac{2\sqrt{k}}{\beta_* \omega y}, \frac{500\nu}{\omega y^2}\right), 100\right)^2\right]. \tag{A3}$$

Finally, the function F_3 aims at preventing the limitation of the eddy viscosity for rough wall flows. This extension was developed by Hellsten et al. (1997) and is written as:

$$F_3 = 1 - \tanh\left[\min\left(\frac{150\nu}{\omega y^2}, 10\right)^4\right]. \tag{A4}$$

By default, F_3 is deactivated and equal to 1.

The model constants α_k is obtained from two other constants α_{k1} and α_{k2} using the blending function F_1 as:

$$\alpha_k = F_1(\alpha_{k1} - \alpha_{k2}) + \alpha_{k2}\,. \tag{A5}$$

The same applies for α_ω with the constants $\alpha_{\omega 1}$ and $\alpha_{\omega 2}$, for β with β_1 and β_2 and for γ with γ_1 and γ_2 . It means than α_k, α_ω and β are not really constants as their values vary in space depending on the distance to the nearest wall. The different constant of the model are $\beta_* = 0.09$, $\alpha_{k1} = 0.85$, $\alpha_{k2} = 1$, $\alpha_{\omega 1} = 0.5$, $\alpha_{\omega 2} = 0.856$, $\beta_1 = 0.075$, $\beta_2 = 0.0828$, $\gamma_1 = 5/9$, $\gamma_2 = 0.44$ $a_1 = 0.31$, $b_1 = 1$, $c_1 = 10$.

Appendix B: Derivation of Darcy-Weissbach source term

This appendix provide more detail on the source term used in Section 5 to take into account the friction due to the presence of the lateral walls. For the simplification of the notation and the demonstration, the flow is supposed to be uniform and

unidirectional in the x-direction, the transverse direction is the y-direction, and there is no pressure gradient. The velocity field simplifies to $\boldsymbol{u} = u(x,y)\boldsymbol{e_x}$ and the momentum equations is written as follows:

$$\rho_f \frac{\partial u}{\partial t} = \frac{\partial \tau_{xy}}{\partial y}\,, \tag{B1}$$

where $\tau_{xy} = (\nu + \nu_t)\partial u/\partial y$ is the total stress due to viscous effect and turbulence. Integrating this equations over the flume width $y \in [0, W_c]$ yields the following equation:

$$\int_0^{W_c} \rho_f \frac{\partial u}{\partial t} dy = \int_0^{W_c} \frac{\partial \tau_{xy}}{\partial y} dy\,, \tag{B2}$$

and then,

$$\rho_f W_c \frac{\partial \overline{u}^y}{\partial t} = \tau_{xy}|_{y=W_c} - \tau_{xy}|_{y=0}\,, \tag{B3}$$

with $\overline{u}^y = 1/W_c \int u dy$ and $\tau_{xy}|_{y=W_c} = -\tau_{xy}|_{y=0} = -\tau_{wall}$. Dividing this equation B3 by $\rho_f W_c$ yields:

$$\frac{\partial \overline{u}^y}{\partial t} = -2\frac{\tau_{wall}}{\rho_f W_c}\,. \tag{B4}$$

Now, replacing τ_{wall} with the Darcy-Weissbach equation (Eq. 33), the source term from equation 35 is retrieved $F_{walls} = -f|u|u/4W_c$.

Appendix C: Dune migration, supplementary material

The position of the dune, height and length were estimated as in the work of Kiki Sandoungout (2019). When the dune does not have a sharp crest, it was found difficult experimentally to identify the precise x-location corresponding to the top of the dune. Instead, it was chosen to track the dune migration using the coordinate x_h, defined from the abscissa of the mid-height of the downstream face. For the length of the dune, it was chosen to estimate it from the base of the triangle formed by the two lines approximating the downstream and upstream faces. This method allows to avoid artifacts in the profile that can occur at the foot of the upstream or downstream face. The definitions of x_h and the dune height and length are summarized in the schematic shown in Figure C1.

As stated in Section 5, the migration of the dune is affected by various parameters of the model. A first important parameter is the mesh resolution and in particular the near bed resolution. A poor resolution leads to an underestimate of the bed shear stress. Table C1 summarize the characteristics of four different meshes used in a sensitivity analysis.

The bed motion is deactivated to study the effect of mesh resolution on the bed shear stress without morphodynamics and each simulation is run for 10 seconds in order to reach a stationary state. Figure C2 shows the stream-wise component of the bed shear stress obtained with the four meshes presented in table C1. The maximum friction velocity consistently occurs slightly upstream of the crest. Its position is sensitive to mesh resolution, shifting farther upstream as the mesh is refined. Poor mesh resolution leads to an underestimation of the maximum friction velocity near the dune crest, which can slow the migration

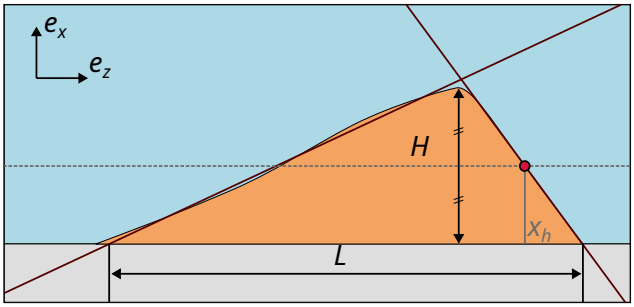

Figure C1. Schematic showing how the dune's characteristics are defined. The dune's position is tracked using the coordinate x_h corresponding to the abscissa of the mid-height of the downstream side of the dune. The dune's length is the base of the triangle formed by the lines approximating the downstream and upstream slopes and the rigid bed.

meshes	M0	M1	M2	M3
n_x	300	500	1000	1100
n_z	30	50	70	80
z_1 in mm	1.037	0.359	0.257	0.142

Table C1. Characteristics of the four mesh used in the numerical study of dune migration. Ranging from coarse mesh M0 to fine mesh M3. The domain length is 800 mm and domain height is 90 mm for all meshes. n_x and n_z are the number of cells in x-direction and z-direction, respectively and z_1 distance from first cell center to wall boundary.

process in morphodynamics simulations. Using a fine mesh also reveals additional flow features near the dune extremities. For instance, a small recirculation develops at the upstream foot of the dune, and the friction velocity decreases at the transition between the downstream slope and the flat bed.

The results presented in Figure C3 show the bed level after 10 seconds of migration for L_{sat} values ranging from 0 mm to 20mm. The light-blue curve corresponds to the case without saturation. The results indicate that introducing a finite saturation length accelerates the migration process. It is also observed that using an excessively large value of $L_{sat} = 20\,mm$ slows down the migration. Saturation acts as a spatial filter and smooths out the maximum of $\boldsymbol{q_{sat}}$. For very large value of L_{sat} this results in an underestimation of $\boldsymbol{q_b}$ and the migration velocity is reduced.

Acknowledgements. This work was carried out within the framework of the OXALIA Chair, supported by the Fondation Grenoble INP thanks to the patronage of Artelia, and is affiliated with LEGI.

Various graphics presented in this work were produced using the Python package *fluidfoam* (Bonamy et al., 2025).

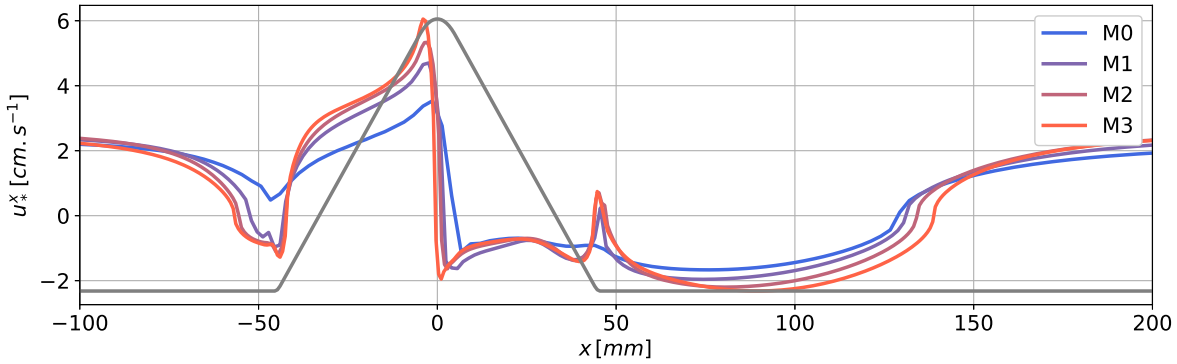

Figure C2. Comparison of stream wise component of friction velocity obtained for 3 different bottom boundary conditions (smooth bed, Fuhrman and Knopp) and 4 different mesh resolutions (M0, M1, M2 and M3).

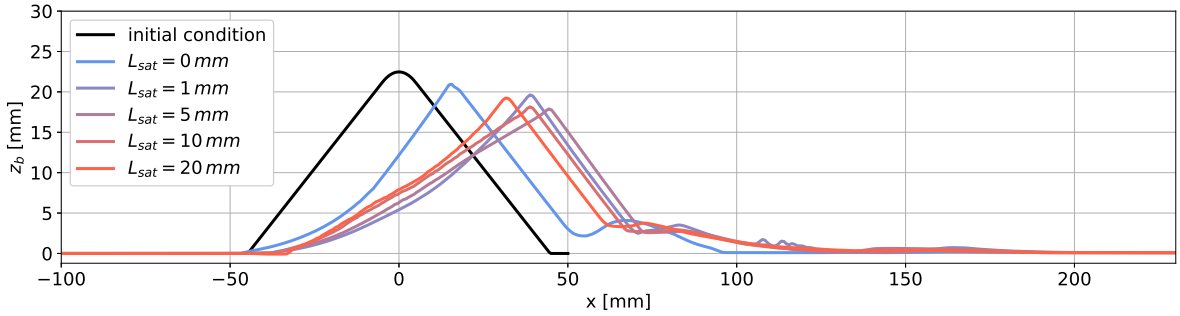

Figure C3. Bed elevation obtained with different saturation length values, ranging from $L_{sat} = 0\,mm$ (no saturation) to $L_{sat} = 20\,mm$.

References

Amoudry, L., Hsu, T.-J., and Liu, P. L.-F.: Schmidt number and near-bed boundary condition effects on a two-phase dilute sediment transport model, J. Geophys. Res.: Oceans, 110, https://doi.org/https://doi.org/10.1029/2004JC002798, 2005.

Baykal, C., Sumer, B. M., Fuhrman, D. R., Jacobsen, N. G., and Fredsøe, J.: Numerical investigation of flow and scour around a vertical circular cylinder, Philos. Trans. R. Soc. London, Ser. A, 373, 20140 104, https://doi.org/https://doi.org/10.1098/rsta.2014.0104, 2015.

Benoit, M., Aelbrecht, D., Bellue, G., Luck, M., and Violeau, D.: Propagation des houles et des surcotes extrêmes vers les côtes et estuaires Apports de la modélisation numérique, La Houille Blanche, 88, 86–89, https://doi.org/https://doi.org/10.1051/lhb/2002029, 2002.

Bonamy, C., Chauchat, J., Clemencot, Q., Puig Montellà, E., Mathieu, A., Chassagne, R., Renaud, M., Höhn, P., Bernard, A., Gonçalves, G., Skorlic, M., and Nikiteas, I.: fluiddyn/fluidfoam: v0.2.9, https://doi.org/10.5281/zenodo.14893673, 2025.

Brownlie, W. R.: Prediction of flow depth and sediment discharge in open channels., https://api.semanticscholar.org/CorpusID:109763694, 1983.

Camenen, B.: Settling velocity of sediments at high concentrations, in: Sediment and Ecohydraulics, vol. 9 of *Proceedings in Marine Science*, pp. 211–226, 2008.

Camenen, B. and Larson, M.: A general formula for non-cohesive bed load sediment transport, Estuarine Coastal Shelf Sci., 63, 249–260, https://doi.org/https://doi.org/10.1016/j.ecss.2004.10.019, 2005.

Celik, I. and Rodi, W.: Modeling suspended sediment transport in nonequilibrium situations, J. Hydraul. Eng., 114, 1157–1191, https://doi.org/https://doi.org/10.1061/(ASCE)0733-9429(1988)114:10(1157), 1988.

Charru, F.: Selection of the ripple length on a granular bed sheared by a liquid flow, Phys. Fluids, 18, https://doi.org/https://doi.org/10.1063/1.2397005, 2006.

Charru, F., Andreotti, B., and Claudin, P.: Sand ripples and dunes, Annu. Rev. Fluid Mech., 45, 469–493, https://doi.org/https://doi.org/10.1146/annurev-fluid-011212-140806, 2013.

Chatterjee, S., Ghosh, S., and Chatterjee, M.: Local scour due to submerged horizontal jet, J. Hydraul. Eng., 120, 973–992, https://doi.org/https://doi.org/10.1061/(ASCE)0733-9429(1994)120:8(973), 1994.

Chauchat, J., Cheng, Z., Nagel, T., Bonamy, C., and Hsu, T.-J.: SedFoam-2.0: a 3-D two-phase flow numerical model for sediment transport, Geosci. Model Dev., 10, 4367–4392, https://doi.org/https://doi.org/10.5194/gmd-10-4367-2017, 2017.

Chiew, Y.-M. and Melville, B. W.: Local scour around bridge piers, J. Hydraul. Res., 25, 15–26, https://doi.org/https://doi.org/10.1080/00221688709499285, 1987.

Cunge, J. A., M, H. F., and Verwey, A.: Practical aspects of computational river hydraulics, [Monographs and surveys in water resources engineering] 3, Pitman Advanced Pub. Program, ISBN 0-273-08442-9, 1980.

Duran Vinent, O., Andreotti, B., Claudin, P., and Winter, C.: A unified model of ripples and dunes in water and planetary environments, Nat. Geosci., 12, 345–350, https://doi.org/10.1038/s41561-019-0336-4, 2019.

Einstein, H. A.: Formulas for the transportation of bed load, Trans. Am. Soc. Civil Eng., 107, 561–577, https://doi.org/10.1061/TACEAT.0005468, 1942.

Engelund, F. and Fredsøe, J.: A sediment transport model for straight alluvial channels, Hydrol. Res., 7, 293–306, 1976.

Exner, F. M.: Zur physik der dünen, Hölder Sitzber Akad. Wiss Wien., 1920.

Fang, H.-W. and Rodi, W.: Three-dimensional calculations of flow and suspended sediment transport in the neighborhood of the dam for the Three Gorges Project (TGP) reservoir in the Yangtze River, J. Hydraul. Res., 41, 379–394, https://doi.org/10.1080/00221680309499983, 2003.

Fredsoe, J. and Deigaard, R.: Mechanics of coastal sediment transport, vol. 3, World scientific publishing company, https://doi.org/https://doi.org/10.1142/1546, 1992.

Gilletta, A., Chauchat, J., Bonamy, C., Robert, M., and Hsu, T.-J.: Scour around a wind turbine pile using a two-phase flow turbulence-resolving model, in: 2024 Ocean Sciences Meeting, AGU, 2024.

Goutal, N. and Maurel, F.: A finite volume solver for 1D shallow-water equations applied to an actual river, Int. J. Numer. Methods Fluids, 38, 1–19, https://doi.org/10.1002/fld.201, 2002.

Greenshields, C. and Weller, H.: Notes on Computational Fluid Dynamics: General Principles, CFD Direct Ltd, Reading, UK, 2022.

Hager, W. H.: Du Boys and sediment transport, J. Hydraul. Res., 43, 227–233, https://doi.org/10.1080/00221680509500117, 2005.

Hellsten, A., Laine, S., Hellsten, A., and Laine, S.: Extension of the k-omega-SST turbulence model for flows over rough surfaces, in: 22nd atmospheric flight mechanics conference, p. 3577, https://doi.org/10.2514/6.1997-3577, 1997.

Hervouet, J.-M.: TELEMAC, a hydroinformatic system, La houille blanche, pp. 21–28, https://doi.org/https://doi.org/10.1051/lhb/1999029, 1999.

Hervouet, J.-M.: Hydrodynamics of free surface flows: modelling with the finite element method, John Wiley & Sons, https://doi.org/10.1002/9780470319628, 2007.

Hjelmfelt, A. T. and Lenau, C. W.: Nonequilibrium transport of suspended sediment, J. Hydraul. Div., 96, 1567–1586, 1970.

Hu, Y., Li, D., Deng, J., Yue, Y., Zhou, J., Yang, C., Zheng, N., and Li, Y.: Dune development dominates flow resistance increase in a large dammed river, Water Resour. Res., 60, e2023WR036 660, https://doi.org/10.1029/2023WR036660, 2024.

Issa, R. I.: Solution of the implicitly discretised fluid flow equations by operator-splitting, J. Comput. Phys., 62, 40–65, https://doi.org/https://doi.org/10.1016/0021-9991(86)90099-9, 1986.

Jacobsen, N. G.: A full hydro-and morphodynamic description of breaker bar development, Ph.D. thesis, ISBN 978-87-90416-64-5, 2011.

Jacobsen, N. G.: Mass conservation in computational morphodynamics: uniform sediment and infinite availability, Int. J. Numer. Methods Fluids, 78, 233–256, https://doi.org/10.1002/fld.4015, 2015.

Jasak, H. and Tukovic, Z.: Automatic mesh motion for the unstructured finite volume method, Trans. FAMENA, 30, 1–20, 2006.

Jasak, H., Jemcov, A., Tukovic, Z., et al.: OpenFOAM: A C++ library for complex physics simulations, in: International workshop on coupled methods in numerical dynamics, vol. 1000, pp. 1–20, Dubrovnik, Croatia), 2007.

Kennedy, J. F.: The mechanics of dunes and antidunes in erodible-bed channels, J. Fluid Mech., 16, 521–544, https://doi.org/10.1017/S0022112063000975, 1963.

Kiki Sandoungout, S.: Caractérisation de la morphologie des dunes dans des écoulements unidirectionnels et alternatifs, Ph.D. thesis, Université de Bretagne occidentale - Brest, https://theses.hal.science/tel-02453140, 2019.

Launder, B. E. and Spalding, D. B.: The numerical computation of turbulent flows, in: Numerical prediction of flow, heat transfer, turbulence and combustion, pp. 96–116, Elsevier, https://doi.org/https://doi.org/10.1016/B978-0-08-030937-8.50016-7, 1983.

Lesser, G. R., Roelvink, J. v., van Kester, J. T. M., and Stelling, G.: Development and validation of a three-dimensional morphological model, Coastal Eng., 51, 883–915, https://doi.org/10.1016/j.coastaleng.2004.07.014, 2004.

Liu, X. and García, M. H.: Three-dimensional numerical model with free water surface and mesh deformation for local sediment scour, J. Waterw. Port. Coast., 134, 203–217, https://doi.org/10.1061/(ASCE)0733-950X(2008)134:4(203), 2008.

Lyn, D. A.: A similarity approach to turbulent sediment-laden flows in open channels, J. Fluid Mech., 193, 1–26, https://doi.org/10.1017/S0022112088002034, 1988.

Marchesiello, P., Benshila, R., Almar, R., Uchiyama, Y., McWilliams, J. C., and Shchepetkin, A.: On tridimensional rip current modeling, Ocean Modell., 96, 36–48, https://doi.org/10.1016/j.ocemod.2015.07.003, 2015.

Marieu, V., Bonneton, P., Foster, D. L., and Ardhuin, F.: Modeling of vortex ripple morphodynamics, J. Geophys. Res., 113, 2007JC004 659, https://doi.org/10.1029/2007JC004659, 2008.

Martino, R. G., Ciani, F. G., Paterson, A., and Piva, M. F.: Experimental study on the scour due to a water jet subjected to lateral confinement, Eur. J. Mech. B-Fluid, 75, 219–227, https://doi.org/https://doi.org/10.1016/j.euromechflu.2018.10.009, 2019.

McOwen, R. C.: Partial differential equations : methods and applications, Upper Saddle River, N.J. : Prentice Hall, 1996.

Menter, F. R.: Two-equation eddy-viscosity turbulence models for engineering applications, AIAA J., 32, 1598–1605, https://doi.org/10.2514/3.12149, 1994.

Meyer-Peter, E. and Müller, R.: Formulas for bed-load transport, in: IAHSR 2nd meeting, Stockholm, appendix 2, IAHR, 1948.

Miedema, S.: An analytical method to determine scour, WEDA XXVIII & Texas A&M, 39, 8–11, 2008.

Muste, M., Yu, K., Fujita, I., and Ettema, R.: Two-phase versus mixed-flow perspective on suspended sediment transport in turbulent channel flows, Water Resour. Res., 41, https://doi.org/10.1029/2004WR003595, 2005.

Nagel, T., Chauchat, J., Bonamy, C., Liu, X., Cheng, Z., and Hsu, T.-J.: Three-dimensional scour simulations with a two-phase flow model, Adv. Water Resour., 138, 103 544, https://doi.org/https://doi.org/10.1016/j.advwatres.2020.103544, 2020.

Nielsen, P.: Coastal bottom boundary layers and sediment transport, vol. 4, World scientific, 1992.

Paola, C. and Voller, V. R.: A generalized Exner equation for sediment mass balance, J. Geophys. Res.: Earth Surf., 110, https://doi.org/10.1029/2004JF000274, 2005.

Patankar, S. V. and Spalding, D. B.: A calculation procedure for heat, mass and momentum transfer in three-dimensional parabolic flows, in: Numerical prediction of flow, heat transfer, turbulence and combustion, pp. 54–73, Elsevier, https://doi.org/10.1016/B978-0-08-030937-8.50013-1, 1983.

Rauter, M. and Kowalski, J.: OpenFOAM-avalanche 2312: depth-integrated models beyond dense-flow avalanches, Geosci. Model Dev., 17, 6545–6569, https://doi.org/10.5194/gmd-17-6545-2024, 2024.

Recking, A.: A comparison between flume and field bed load transport data and consequences for surface-based bed load transport prediction, Water Resour. Res., 46, https://doi.org/10.1029/2009WR008007, 2010.

Renaud, M., Bonamy, C., Chauchat, J., and Bertrand, O.: SedFoam/sedExnerFoam: Release 2412, https://doi.org/10.5281/zenodo.15535486, 2025.

Ribberink, J. S.: Bed-load transport for steady flows and unsteady oscillatory flows, Coast. Eng., 34, 59–82, https://doi.org/10.1016/S0378-3839(98)00013-1, 1998.

Richardson, J. and Zaki, W.: The sedimentation of a suspension of uniform spheres under conditions of viscous flow, Chem. Eng. Sci., 3, 65–73, https://doi.org/10.1016/0009-2509(54)85015-9, 1954.

Roulund, A., Sumer, B. M., Fredsøe, J., and Michelsen, J.: Numerical and experimental investigation of flow and scour around a circular pile, J. Fluid Mech., 534, 351–401, https://doi.org/10.1017/S0022112005004507, 2005.

Rubey, W.: Equilibrium-conditions in debris-laden streams, EOS Trans. Am. Geophys. Union, 14, 497–505, https://doi.org/https://doi.org/10.1029/TR014i001p00497, 1933.

Shields, A. F.: Anwendung der Ähnlichkeitsmechanik und der Turbulenzforschung auf die Geschiebebewegung, Ph.D. thesis, 1936.

Song, Y., Xu, Y., Ismail, H., and Liu, X.: Scour modeling based on immersed boundary method: A pathway to practical use of three-dimensional scour models, Coastal Eng., 171, 104 037, https://doi.org/10.1016/j.coastaleng.2021.104037, 2022.

Soulsby, R. and Whitehouse: Threshold of Sediment Motion in Coastal Environments, in: Proceedings of the 13th Australasian Coastal and Ocean Engineering Conference and the 6th Australasian Port and Harbour Conference, vol. 1, pp. 145–150, Christchurch, N.Z., ISBN 978-0-908993-15-4, 1997.

Stokes, G. G.: Mathematical and physical papers, vol. 3, Cambridge University Press, https://doi.org/10.1017/CBO9780511702297, 1901.

Swamee, P. K. and Jain, A. K.: Explicit equations for pipe-flow problems, J. Hydraul. Div., 102, 657–664, https://doi.org/10.1061/JYCEAJ.0004542, 1976.

Tukovic, Z. and Jasak, H.: Simulation of free-rising bubble with soluble surfactant using moving mesh finite volume/area method, in: Proceedings of 6th International Conference on CFD in Oil & Gas, Metallurgical and Process Industries, no. CFD08-072, 2008.

van der Sande, W., Roos, P., Gerkema, T., and Hulscher, S.: Nonlinear modeling of river dunes: Insights in long-term evolution of dune dimensions and form roughness, Geomorphology, p. 109649, https://doi.org/10.1016/j.geomorph.2025.109649, 2025.

Van Rijn, L. C.: Sediment transport, part I: bed load transport, J. Hydraul. Eng., 110, 1431–1456, https://doi.org/10.1061/(ASCE)0733-9429(1984)110:10(1431), 1984.

van Rijn, L. C.: Sediment Transport, Part II: Suspended Load Transport, 110, 1613–1641, https://doi.org/10.1061/(ASCE)0733-9429(1984)110:11(1613), 1984.

Warner, J. C., Sherwood, C. R., Signell, R. P., Harris, C. K., and Arango, H. G.: Development of a three-dimensional, regional, coupled wave, current, and sediment-transport model, Comput. Geosci., 34, 1284–1306, https://doi.org/10.1016/j.cageo.2008.02.012, 2008.

Warren, I. and Bach, H.: MIKE 21: a modelling system for estuaries, coastal waters and seas, Environ. Softw., 7, 229–240, https://doi.org/doi.org/10.1016/0266-9838(92)90006-P, 1992.

Wilcox, D. C. et al.: Turbulence modeling for CFD, vol. 2, DCW industries La Canada, CA, 1998.

Zanke, U.: On the influence of turbulence on the initiation of sediment motion, Int. J. Sediment Res., 18, 17–31, 2003.

Zhou, L.: Numerical modelling of scour in steady flows, Ph.D. thesis, http://www.theses.fr/2017LYSEC015/document, 2017.